Physicochemical and tribological comparison of bio- and halogen-based ionic liquid lubricants

Md Hafizur Rahman[a], Ting Liu[b], Tatianna Macias[a], Manoranjan Misra[c], Manish Patel[d], Ashlie Martini[b], Pradeep L. Menezes[a]

[a]Department of Mechanical Engineering, University of Nevada-Reno, Reno, NV 89557, USA
[b]Department of Mechanical Engineering, University of California, Merced, CA 95343, USA
[c]Department of Chemical & Materials Engineering, University of Nevada-Reno, Reno, NV 89557, USA
[d]Nano Additive Technology Inc., Austin, TX 78705, USA

*corresponding author: Email: [a] pmenezes@unr.edu

Abstract

The friction and wear behavior of bio-based trihexyltetradecylphosphonium saccharinate [P6,6,6,14][Sacc] and halogen-based trihexyltetradecylphosphonium bis(trifluoromethylsulfonyl) amide [P6,6,6,14][NTF2] ionic liquids (ILs) were studied to understand their lubrication mechanisms at steel sliding interfaces. The physicochemical and tribological properties of the ILs were characterized over a wide temperature range (10-120 °C) to reflect the conditions present in wind turbine applications. Friction increased with increasing temperature for both ILs. At any temperature, [P6,6,6,14][Sacc] had significantly higher viscosity that provided thicker lubricant films and, in turn, better friction and wear protection than the halogen-based [P6,6,6,14][NTF2]. [P6,6,6,14][Sacc] also had lower density, comparable thermal stability, more favorable wettability, and better corrosion performance than [P6,6,6,14][NTF2]. Simulations showed that the cohesion interaction energy was stronger for [P-Sacc] due to its smaller anion-cation distance. The higher viscosity and stronger cohesion of [P6,6,6,14][Sacc] than [P6,6,6,14][NTF2] contributed to the ability of the bio-based IL to form an effective adsorption film that reduced friction and wear across a range of temperatures.

.....

Keywords

Ionic liquids, bio-based lubricants, friction, wear, cohesion, phosphonium

Nomenclature

[P6,6,6,14][Sacc]	Trihexyltetradecylphosphonium saccharinate, [P-Sacc]
[P6,6,6,14][NTF2]	Trihexyltetradecylphosphonium bis(trifluoromethylsulfonyl) amide, [P-NTF2]
[P6,6,6,14][Cl]	Trihexyltetradecylphosphonium chloride
DCM	Dichloromethane
$CDCl_3$	Deuterated chloroform
TMS	Tetramethylsilane

Highlights:

- Two ionic liquids were characterized across a wide range of temperatures
- [P6,6,6,14][Sacc] and [P6,6,6,14][NTF2] were thermally stable between 10 to 120 °C
- Friction and wear for bio-based [P6,6,6,14][Sacc] were lower than for [P6,6,6,14][NTF2]
- The bio-based IL had higher viscosity, lower density, and more favorable wettability
- [P6,6,6,14][Sacc] resulted in less corrosion on steel than [P6,6,6,14][NTF2]

Graphical Abstract

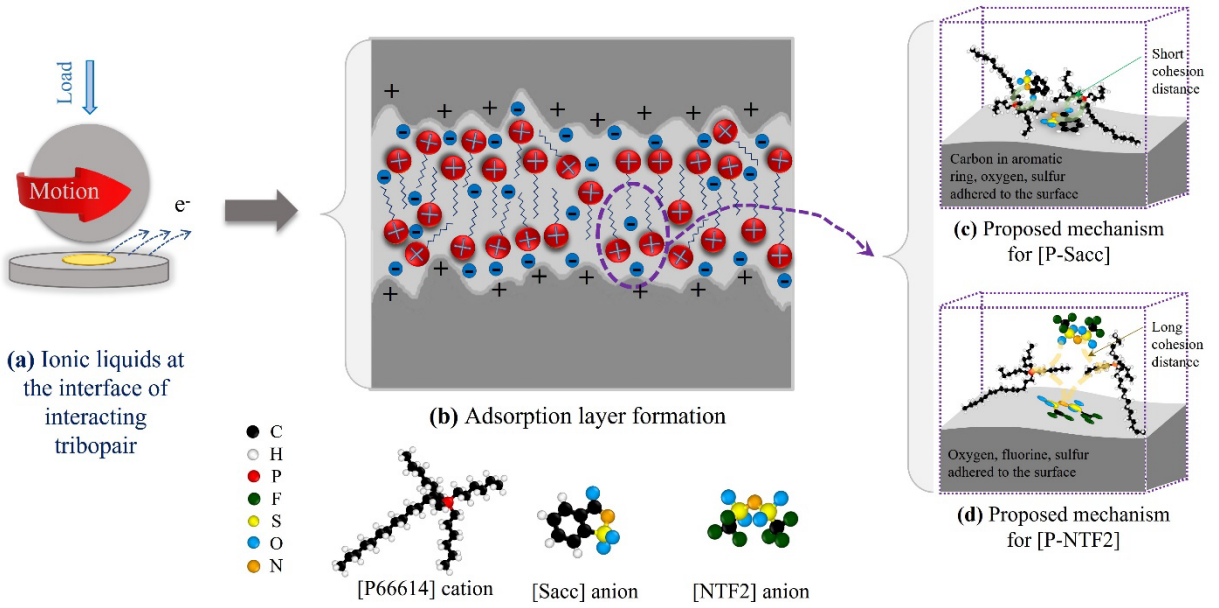

.....

1. Introduction

Clean energy generation is an important global goal due to climate change [1]. As such, there have been significant efforts in recent decades to replace fossil resources with renewables to reduce the carbon footprint [2, 3]. Wind turbines play a crucial role in generating alternative energy [4], and the US Department of Energy has a goal of producing 20% of the nation's electricity from wind turbines by 2030 [5]. To reach this goal, research is needed to improve gearbox efficiency by optimizing lubrication for modern wind turbines [6, 7]. Bio-based lubricants could play a vital role in these efforts.

In a wind turbine, the gearbox ensures adequate rotational speed for energy generation. However, the frictional loss between gears causes significant power loss in wind turbines [8], and the high maintenance and repair cost of wind turbines is mostly due to the gearbox. The major purpose of lubricants in the gearbox is to reduce friction and wear. In other words, the energy consumption in wind turbines due to friction and wear can be minimized with effective lubrication. Over the past two decades, a novel class of lubricants, ionic liquids (IL), has been investigated for wind turbine applications due to their good thermal stability, low vapor pressure, load-carrying capability, and physicochemical properties [9-16].

Many researchers have investigated the friction reduction mechanisms for wind turbine gearboxes using tribological studies under simulated conditions [4, 6, 17-20]. In such studies, phosphonium-based room temperature ionic liquids (P-RTILs) have received significant attention for their promising tribological performance as neat lubricants or lubricant additives [18, 19]. For example, trihexyltetradecylphosphonium bis(trifluoromethylsulfonyl) amide [P6,6,6,14][NTF2] was recently shown to exhibit tribological performance superior to other P-RTILs [6, 19]. However, most of the P-RTILs studied so far are non-bio-based and therefore can have a negative environmental impact [11]. As a result, tribological studies of bio-based P-RTILs for wind turbine applications are necessary to advance research in the direction of sustainable energy generation. Moreover, many P-RTIILs contain halogens that initiate corrosion, which is a drawback for ILs such as [P6,6,6,14][NTF2] [11, 21]. Therefore, tribological studies are needed specifically for bio-based, halogen-free IL lubricants.

Previous studies on P-RTILs have been carried out mostly at room temperature. In contrast, the operating ambient temperature of wind turbines can vary from -30 °C to 50 °C, depending on their location and altitude [22, 23]. The maximum operating temperature of the gearbox can be much higher under continuous operation. As per the 'Application requirements for wind turbine gearbox' recommended by the National Renewable Energy Laboratory (NREL), the maximum oil sump temperature in a wind turbine gearbox should be about 121 °C [23]. On the other hand, for extreme cold weather, a sump heater is needed to heat the oil to 5 °C above its pour point so the oil will circulate freely during start up [23]. Therefore, lubricants used for wind turbine applications need to be operable over a wide temperature range, from below room temperature to nearly 120 °C, and tribological testing of P-RTILs should evaluate this same range.

In our current investigation, we developed a bio-based IL, trihexyltetradecylphosphonium saccharinate ([P6,6,6,14][Sacc]), derived from sodium saccharine, an artificial sweetener compound that is edible, biodegradable, and eco-friendly [24]. We hypothesized that bio-based [P6,6,6,14][Sacc] could provide better lubrication performance over a wide temperature range than the halogen-based [P6,6,6,14][NTF2]. To test this hypothesis, the physicochemical, rheological, and wetting behavior of bio-derived [P6,6,6,14][Sacc] were compared with [P6,6,6,14][NTF2] on steel surfaces across a range of temperatures. Molecular dynamics (MD) simulations were then used to analyze the wetting behavior of the ILs in terms of adhesion and cohesion interaction energies. The lubrication mechanisms of these ILs were explained based on their inherent physicochemical properties and interfacial interaction chemistry, with input from

the MD simulations. It was observed that viscosity, wettability, ion structure, and active elements contributed to the formation of adsorption layers on the steel surfaces and dictated the lubrication mechanism. The results of this study will be beneficial for the potential use of bio-based P-RTIL in wind turbines and other high-temperature applications.

2. Materials and Methods

2.1 Materials

Trihexyltetradecylphosphonium bis(trifluoromethylsulfonyl)amide [P6,6,6,14][NTF2], CAS number: 460092-03-9; trihexyltetradecylphosphonium chloride [P6,6,6,14][Cl], CAS number: 258864-54-9; saccharine sodium salt hydrate (CAS number: 6155-57-3), and Dichloromethane (DCM) (CAS number: 75-09-2) were purchased from Millipore Sigma MO, USA. The AISI 52100 stainless steel rod with 12' in length and 25 mm diameter, and AISI 440C stainless steel spherical balls of 6.35 mm diameter were purchased from McMaster Carr, USA.

2.2 Ionic liquid synthesis:

Bio-based [P6,6,6,14][Sacc] (chemical formula: $[C_{32}H_{58}P][C_7H_5NO_3S]$) was synthesized using [P6,6,6,14][Cl] and saccharine sodium salt hydrate through an ion exchange reaction [9, 25, 26]. Deionized (DI) water and Dichloromethane were used during the washing steps after the ion exchange reaction. The water with dissolved salt (NaCl) and the Dichloromethane (DCM) with dissolved IL were separated using a separating funnel to carry out the density-based separation process. The DCM with washed IL was heated inside a vacuum furnace at 80±5 °C for 6 h. DCM (boiling point ~40 °C) and residual moisture content (boiling point ~80 °C under vacuum) were evaporated from the solution, and the dried IL was stored at room temperature (RT) inside a humidity-controlled desiccator (10±5%RH).

Since this manuscript compares two ionic liquids with the same cation, [P6,6,6,14][Sacc] and [P6,6,6,14][NTF2], for convenience they will subsequently be referred to simply as [P-Sacc] and [P-NTF2].

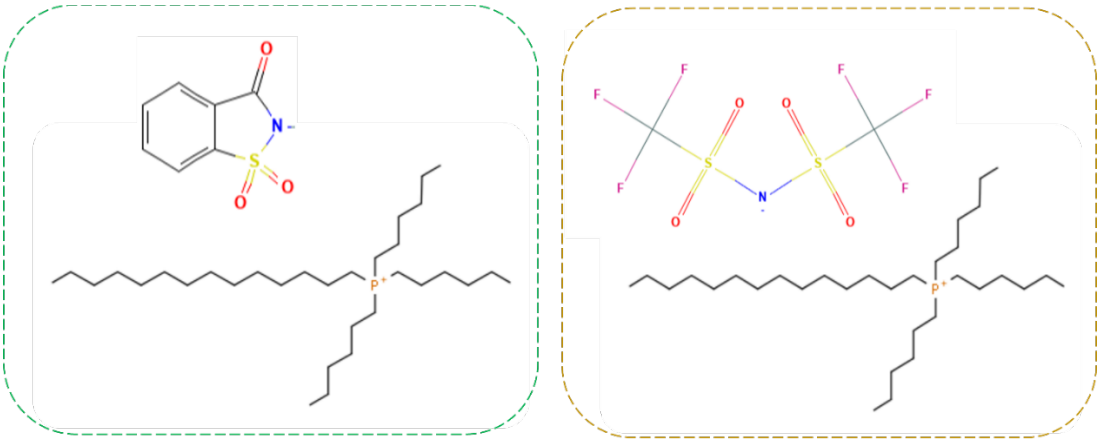

Figure 1. Chemical structures of (a) [P-Sacc] and (b) [P-NTF2].

2.3 Structural characterization

The chemical structures of [P-Sacc] and [P-NTF2] are shown in **Figure 1**. Both ILs were characterized using Fourier Transform Infrared Spectroscopy (FTIR), ^{1}H and ^{13}C Nuclear Magnetic Resonance (NMR) spectroscopy. FTIR analyses were performed for [P-NTF2] and [P-Sacc] using a Nicolet FTIR (Model:

iS™ 380, Thermo Scientific). To analyze each sample, first, the background was collected using OMINIC™ software. Then, one sessile droplet of IL was placed on the pressure tip under the pressure tower to collect the sample spectrum. Further characterization of the ILs was carried out using an Agilent 500-MHz ^{1}H (Figure 4) and 126 MHz ^{13}C NMR spectroscope (Figure S1). Deuterated chloroform ($CDCl_3$ having D, 99.8%+0.05% V/V TMS) was used as the solvent to prepare ~60 mM solution, and 1 mL of the prepared sample was used inside the NMR tube to carry out the analyses. The results were analyzed using MestReNova software.

2.4 Thermogravimetric analyses

In extreme applications, such as in wind turbines, the operating temperature varies significantly. Therefore, the thermal stability of the lubricant is a crucial factor in wind turbines [27]. Particularly, thermal decomposition of the liquid lubricant can lead to component failure and so should be avoided. To understand the decomposition behavior of the studied ILs, thermogravimetric analyses were carried out as per the ASTM E2550-17, with an argon flow rate of 20 mL/min in a Shimadzu TA60 thermogravimetric analyzer at a heating rate of 10 °C/min up to 600 °C. Further, the long-term thermal stability of the ILs was tested through isothermal heating over 10 h, following the method described by Wooster et al. [28] and our recent work [12].

2.5 Viscosity measurements

Viscosity is a crucial lubricant property that is influenced by temperature. Lubricants often fail at high temperatures because the viscosity decreases significantly, leading to reduced film thickness and possible direct contact between the asperities of the tribo-pairs [29]. In contrast, a very high viscosity lubricant at low temperature can increase viscous friction losses in full film lubrication. Therefore, ensuring appropriate viscosity across the entire operating temperature range is important for proper lubrication in extreme conditions. In our experiments, the dynamic viscosity of the ILs was measured in a rotary viscometer (Ametek Brookfield DV2T extra) with spindle no. 29 at 40 rpm, corresponding to a shear rate of 10 s^{-1}. The temperature was maintained using a thermosel assembly, manufactured by Ametek Brookfield.

2.6 Density measurements

Density is another important physical property of lubricants that decreases with temperature. For the same volumetric coverage, a lower density lubricant will have less mass and, therefore, could be preferred in applications for which weight is an important factor. Also, the volumetric thermal expansion coefficient, specific gravity, specific volume, and other important fluid properties can be obtained from density [30, 31]. In the current experiments, the density of the studied ILs was measured using Archimedes principle in a Metler Toledo density measuring instrument (MS104TS/A00).

2.7 Wettability test

Wettability and the ability to stay on a tilted surface are important for lubricants [21]. This behavior is quantified by contact angle. The contact angle represents the wettability of a liquid droplet on a solid surface and is dominated by two forces: (1) adhesion force between the liquid and the solid, and (2) cohesion force within the liquid. The contact angle is typically inversely related to wettability [11]. A droplet contact angle of less than 90° on a steel surface could be considered an indication of good wettability [21, 32]. ILs typically have small contact angles, indicating strong interactions with the surface and could be related to the formation of chemisorbed tribofilms [21]. In the current investigation, the contact angle measurements of the ILs were carried out using a goniometer (Model-260, NJ, USA). A sessile droplet of 5 µl was dropped using a micro-syringe assembly on a AISI 52100 sample, and the contact angles were detected by a 750

FPS superspeed U2 series upgrade kit (p/n 100-12-U2), all manufactured by Rame-hart, NJ, USA. The contact angles of the left side (θ_l) and the right side (θ_r) of the sessile droplet were recorded every 1 seconds interval using Dropimage software, and the average contact angle (θ) was used as an individual test result, as reported in the literature [33]. To ensure repeatability, each test was repeated at least two times, and the average was reported.

2.8 Adhesion-cohesion interaction energy analysis

Classical MD simulations were used to study the adhesion between the P-RTILs and an ideal Fe (111) surface, and cohesion between cations and anions at different temperatures. The models and simulation approach were described in detail in our previous study [34]. Briefly, each simulation had one 5 nm ×5 nm IL droplet on a 25 nm x 25 nm surface comprising five layers of Fe atoms arranged in a body-centered-cubic lattice with (111) orientation. The liquid droplets were constructed using PACKMOL [35] from 120 cations and 120 anions. A snapshot of the initial [P-Sacc] model is shown in **Figure 2(a)**. The interatomic interactions within and between the ILs were described by the OPLS-AA Force field [36] based on LigParGen [37]. For the solid-solid interaction, the Lennard-Jones potential was applied with the parameters ε = 0.2007 eV and σ = 2.4193 Å [38] and a 1.2 nm cutoff. All MD simulations were performed using the open-source Large Atomic/Molecular Massively Parallel Simulation (LAMMPS) package [34, 39] with a timestep of 1 fs. After energy minimization and equilibration at 25°C, the, simulations were run at temperatures of 25°C, 40°C, and 80°C for 10 ns. During the simulation, the IL droplet spread out on the surface, as shown for [P-Sacc] in **Figure 2(b).** The [P-NTF2] model looked similar at the end of the 10 ns simulation.

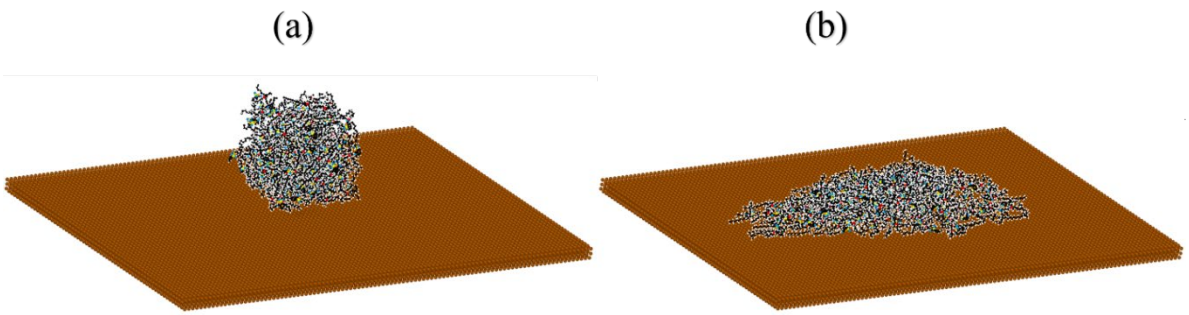

Figure 2. The spreading of [P-Sacc] on an Fe substrate from (a) a cube shape droplet to (b) a relaxed sessile droplet.

2.9 Corrosion tests

During use, a lubricant may oxidize, resulting in corrosion and wear of the friction surfaces. To understand the corrosion behavior of the ILs, ASTM 4048 copper strip corrosion tests were carried out. The samples (10 mm × 6 mm × 3mm) were dipped into the ILs and kept inside a furnace at a temperature of 100±5 ℃ for 24 h. During analyses, the color change of the strips was compared with the ASTM standard corrosion color code. Also, the long-term effect of the ILs on the AISI 52100 steel was studied by covering two steel samples with ILs for 4 weeks. After 28 days, the samples were analyzed using the profilometer to measure any pitting.

2.10 Tribological testing

The friction and wear performance of the ILs was evaluated at five different temperatures (10 °C, 25 °C, 40 °C, 80 °C, 120 °C) at ambient conditions. AISI 52100 steel disks (Rockwell hardness 22.8 HRC) of 5 mm thickness and 25 mm diameter were prepared from the 12' long steel rod. All disk surfaces were mechanically polished using silicon carbide polishing papers (Buehler, IL, USA) of 120, 240, 400, 600, 1000 grit sizes. The average roughness of the disk samples was R_q= 0.1±0.07 µm. The polished samples were ultrasonicated with Acetone for 5 min, dried using an air dryer, and then preserved inside corrosion resistant bags prior to testing. Wear-resistant hard martensitic 440C stainless steel (SS) balls (Rockwell hardness 57-65 HRC) of 6.35 mm diameter were used as the counter bodies.

All tribological tests were performed using the ball-on-disk setup in an Rtec multifunction tribometer (MFT 5000, manufactured by Rtec, CA, USA). Tests below room temperature were run with a chiller-based cooling system (F25, manufactured by Julabo, PA, USA). Tests above room temperature were run with a high-temperature assembly (manufactured by Rtec, CA, USA). Each test was done at a maximum Hertzian contact pressure of 2.74 GPa, following earlier work on wind turbines done by Cigno et al. [19]. The coefficient of friction (COF) was continuously recorded throughout the test duration of one hour. The mean COF was obtained after each test, and the average of at least three tests was used for comparison. The test conditions are summarized in **Table 1**. The wear was measured from profilometer images of the wear tracks on the disks, taken at 10× magnification at 5 different locations on the wear track, using an Rtec profilometer. Then, 2D profiles at different locations along the wear track were extracted to measure the wear area, which was multiplied by the wear track length to obtain the volumetric wear [40, 41].

Table 1. Conditions for the friction and wear tests

Friction pair	AISI 52100/SS 440C
Lubricant	[P-Sacc]/[P-NTF2]
Temperature (°C)	10/25/40/80/120
Load (N)	80
Contact pressure (GPa)	2.7
Speed (m/s)	0.26
Duration (h)	1
Sliding radius (m)	0.16
Sliding distance (km)	0.94

2.11 Scanning Electron Microscopy (SEM) and Energy Dispersive X-Ray Spectroscopy (EDX) analyses:

SEM analyses of the wear track were carried out using the JEOL 7100 field emission SEM equipment. The analyses were performed at a 100× magnification with an accelerating voltage of 15 kV. The surface chemical compositions were analyzed using the energy-dispersive X-ray spectroscopy technique installed on the same instrument.

3 Results and Discussion

3.1 IL composition

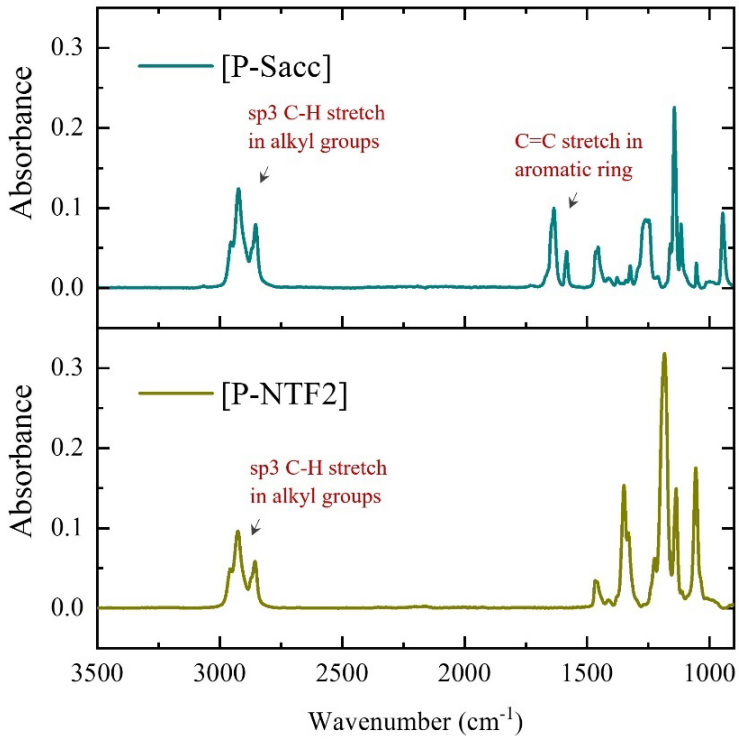

Figure 3. FTIR spectra for **(a)** [P-Sacc] and **(b)** [P-NTF2]

Figure 3 (a-b) show FTIR spectra for [P-Sacc] and [P-NTF2]. The FTIR spectra were analyzed using the five-zone analysis method [42-44], based on the illustrated Glossary of Organic Chemistry [45]. For both ILs, prominent peaks were observed for the alkyl sp^3 C-H bonds. The [P-Sacc] ILs with Saccharinate anions had two additional peaks between 1450-1650 cm^{-1} corresponding to the C=C functional groups present in the aromatic ring; these peaks were absent in the spectrum for [P-NTF2]. The presence of aromatic ring was further confirmed using ^{1}H NMR spectra.

Figure 4 (a) shows the ^{1}H NMR spectrum for the [P-Sacc] where the x-axis is chemical shift (ppm) and the y-axis is the intensity (atomic unit). In the ^{1}H NMR, seven multiplets (A-G) were observed. Three (A, B and C) of these multiplets were in the aromatic region (6-8 ppm) [46]. The integral value for these three multiplets was 4, corresponding to the number of proton nuclei present in the aromatic ring structure of saccharinate anion. Among the other four multiplets, F is located in the methyl group region (-1 to 4) and corresponds to the 4 methyl groups ($-CH_3$) present at the four ends of the cation side chains [46]. D, E and G multiplets are located within the alkyl chain region (1.1-5.2), confirming the 56 proton nuclei present in the four alkyl chain branches of the cation [46].

Figure 4 (b) shows the ^{1}H NMR spectrum for [P-NTF2], which does not have any protons in the anion (NTF2). Similar to [P-Sacc], here the total number of proton nuclei in the cationic structure is 64, with 52 in the alkyl chain (multiplets A-C), and 12 in the methyl groups at the ends of four alkyl chains (multiplet D). Similar spectra were previously reported [47] for trihexyltetradecyl phosphonium cations (with tetrafluoroborate anion). Importantly, the absence of peaks between 6-8 ppm confirms the difference (the aromatic ring structure) between the [P-NTF2] and the synthesized [P-Sacc].

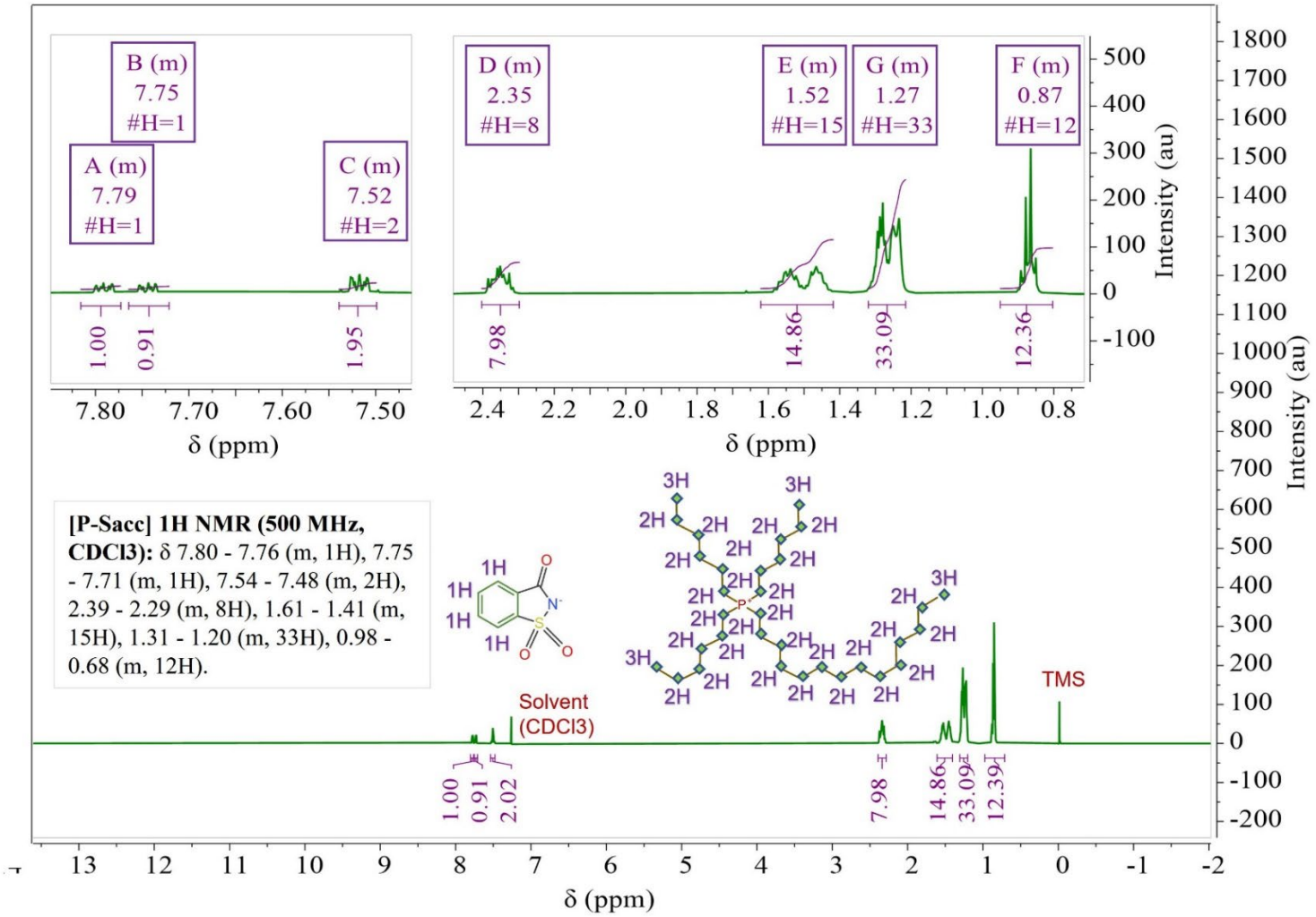

Figure 4 (a). ^{1}H NMR spectra for [P-Sacc]

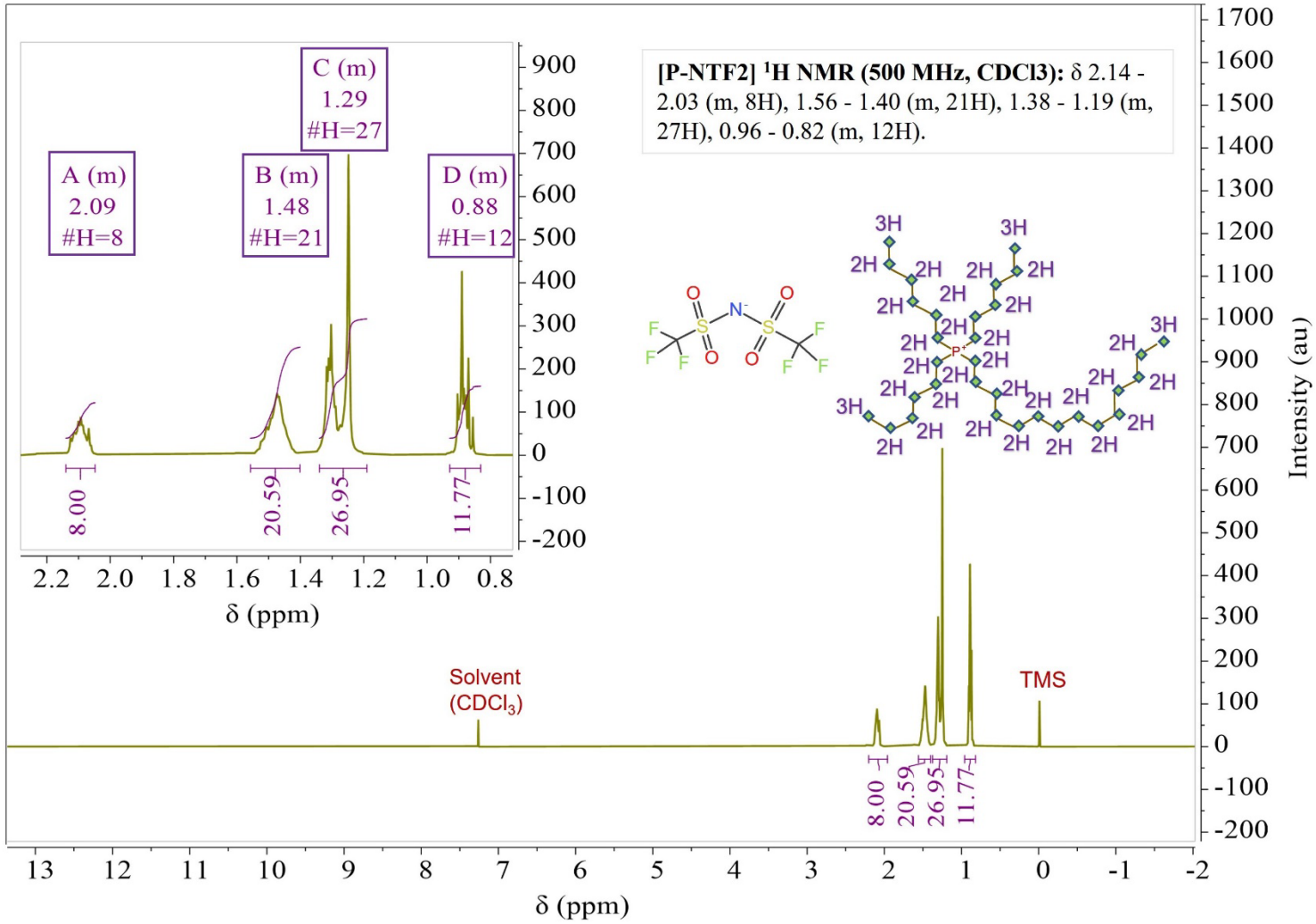

Figure 4 (b). ^{1}H NMR spectra for [P-NTF2]

3.2 Thermal stability

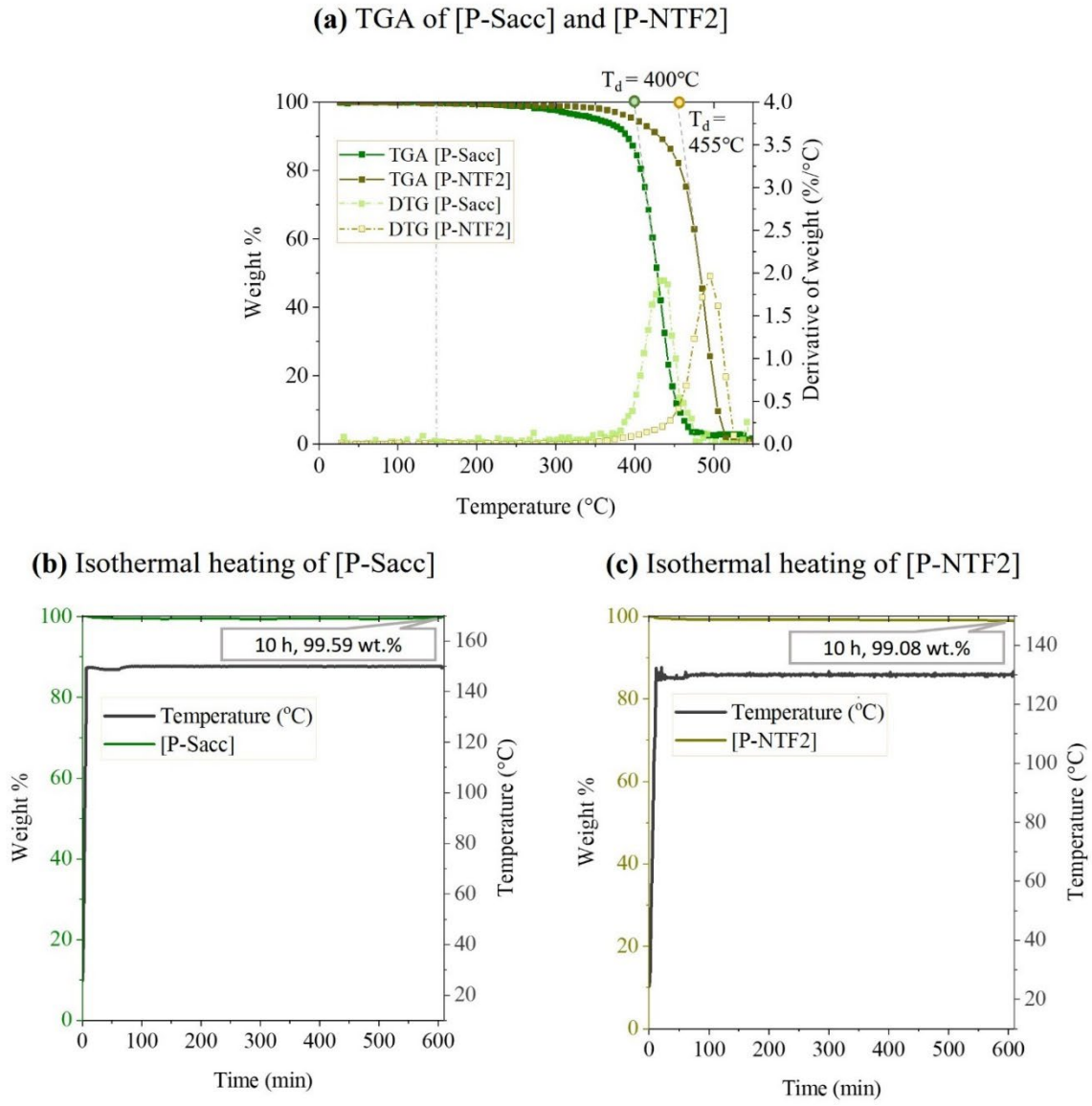

Figure 5 (a). TGA and DTG of [P-Sacc] and [P-NTF2]. Long-term thermal stability of **(b)** [P-Sacc] and **(c)** [P-NTF2].

Figure 5 (a) shows the thermal decomposition of [P-Sacc] and [P-NTF2] reported in terms of loss of wt.% as a function of temperature as well as the results of derivative thermogravimetry (DTG) where the right y-axis is rate of weight loss with temperature in units of %/°C. It is observed that the onset of decomposition (T_d) [42] is 400 °C and 455 °C for [P-Sacc] and [P-NTF2], respectively. These values are comparable to decomposition temperatures for P-RTILs reported previously [11]. From literature [48-51], the bond type and bond dissociation energy in [Sacc] are: C-H 337.2 kJ/mol, C-C 607 kJ/mol, C=O 749 kJ/mol, C-N 770 kJ/mol, C-S 699 kJ/mol, N-S 464 kJ/mol, and S=O 521.7 kJ/mol, while in [NTF2] they are: C-F 536 kJ/mol, C-S 699 kJ/mol, N-S 464 kJ/mol, S=O 521.7 kJ/mol. For different bonds, the bond energy, which is directly proportional to the stability of that bond, also varies. Except for the similar C-S, N-S, and S=O bonds, the C-F bonds in [NTF2] has higher bond energy than the C-H bonds in [Sacc]. This could be attributed to the obvious higher decomposition temperature for [P-NTF2] than [P-Sacc]. It was also reported that the

increase of symmetry and rigidity of the molecule will lead to higher thermal stability for molecules with similar function group and atom compositions [52]. Since [NTF2] is more symmetric than [Sacc], this could also explain the higher thermal decomposition temperature of [P-NTF2] than [P-Sacc]. Although the decomposition temperature of [P-Sacc] is lower than that of [P-NTF2], both [P-Sacc] and [P-NTF2] experience significant decomposition at temperatures higher than 150 ℃. Therefore, both could be considered for applications where the lubricant experiences temperatures less than 150 ℃.

The long-term thermal stability of an IL is important for its use as a lubricant. Per Wooster et al. [28] the temperature at which less than 1% degradation of an IL takes place over 10 h is denoted as $t_{0.99}$ and is considered an indicator of the maximum operating temperature for the IL [28, 53, 54]. In the current investigation, it is important to determine if $t_{0.99}$ is greater than 120 ℃ for both ILs, because the operating temperature of the wind turbine gearbox may reach as high as 120 ℃ during operation [23]. To verify the usability of these ILs for wind turbine applications, [P-Sacc] and [P-NTF2] were held at 150 ℃ for 10 h. At this temperature, over 99% residual wt.% was obtained for [P-Sacc], whereas, for [P-NTF2], the residual wt.% was less than 99%. Therefore, [P-NTF2] was further tested at 130 ℃ for 10 h and the residual wt.% observed was above 99%. **Figure 5 (b-c)** shows the residual wt.% after 10 h of isothermal heating for [P-Sacc] and [P-NTF2], respectively. These results indicate that 120 ℃ is a safe temperature limit for these ILs from the thermal stability point of view.

For cold temperature operation, the ILs should not lose their flowability. This was characterized by the pour point test carried out per the ASTM D97 standard. This test is particularly important for starting wind turbines below room temperature, such as in cold weather conditions. For the pour point test, the P-RTIL samples were cooled down to 5 ℃ using a refrigerator, and then the container was tilted 90 degrees and held for 5 seconds to verify that both P-RTILs were flowable at this condition [23]. The NREL wind turbine gearbox recommendations indicate the use temperature should be 5 ℃ above the pour point [23], so our results show [P-Sacc] and [P-NTF2] can both be used at 10 ℃.

3.3 Specific density, specific gravity, and thermal expansion coefficient

Figure 6 shows the density and specific volume of [P-Sacc] and [P-NTF2] ILs from 25 to 100 ℃. The density of [P-Sacc] at room temperature was 0.997 g/cm^3, whereas [P-NTF2] exhibited 8.73% higher density (1.065 g/cm^3). The difference was 8.18% at 100 ℃, where the density of [P-Sacc] and [P-NTF2] were 0.932 g/cm^3 and 1.015 g/cm^3, respectively. The values for [P-NTF2] are consistent with earlier literature [33]. Density data was used to calculate specific gravity by dividing the IL density by that of water (0.997 g/cc) at 25 ℃. Therefore, [P-NTF2] had a specific gravity value of 1.068, whereas the specific gravity of [P-Sacc] was 0.975. These values of specific gravity for the studied ILs are comparable to that of mineral oil lubricants reported in the literature [55, 56].

The volumetric thermal expansion coefficient (α) was calculated from the following equation [55, 57]:

$$\alpha = \left({}^{1}/_{V}\right)\left({}^{\partial V}/_{\partial T}\right)_{P} \qquad (ii)$$

where V is the specific volume, $\left(\rho = {}^{1}/_{V}\right)$ is the density, and $\left({}^{\partial V}/_{\partial T}\right)$ is the slope of the specific volume vs. temperature under isobaric conditions. For [P-Sacc] and [P-NTF2], the thermal expansion coefficients were 5.6×10^{-4} ℃$^{-1}$ and 6.8×10^{-4} ℃$^{-1}$, respectively. These values are comparable to those reported in the literature for petroleum or mineral oils [56]. The thermal expansion coefficient is useful for calculating density at temperatures other than those measured experimentally.

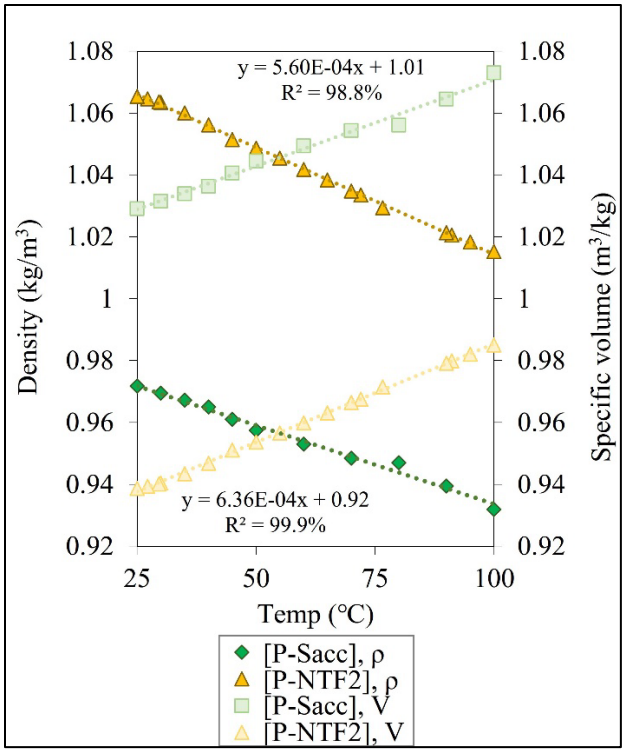

Figure 6. Density and specific volume vs. temperature for [P-Sacc] and [P-NTF2]. The equations correspond to linear fits to the specific volume data ($\partial V/\partial T$) with slopes 5.60×10^{-4} m^3/(kg·°C) and 6.36×10^{-4} m^3/(kg·°C) for [P-Sacc] and [P-NTF2], respectively.

3.4 Viscosity and film thickness

Figure 7 shows the dynamic viscosity for [P-Sacc] and [P-NTF2] on a logarithmic scale from 10 °C to 120 °C. The dynamic viscosity of [P-Sacc] was significantly higher (1460 mPa·s) at room temperature compared to [P-NTF2] (309.4 mPa·s). With an increase in temperature, the viscosity was reduced for both the ILs and, at 120 °C, the dynamic viscosity values for [P-Sacc] and [P-NTF2] were 28.95 mPa·s and 14.04 mPa·s, respectively. Since the change in viscosity with temperature was higher for [P-Sacc] than for [P-NTF2], it had a lower viscosity index value (126) than [P-NTF2] (150).

The minimum film thickness (h_0) was calculated using the following Hamrock and Dowson equation [11, 58-60].

$$h_0 = 3.63R'\left(\frac{U.\eta_0}{E'R'}\right)^{0.68}(\alpha E')^{0.49}\left(\frac{\omega}{E'R'^2}\right)^{-0.073}\left(1-e^{-0.68k}\right) \quad \text{(i)}$$

Here, h_0 = minimum film thickness (m); R'=reduced radius of curvature (m); $\frac{1}{R'}=\frac{1}{R'_x}+\frac{1}{R'_y}$; η_0= dynamic viscosity of the lubricant at the atmospheric pressure (Pa.s); U= velocity of entraining surface (m/s); $U=\frac{U_A+U_B}{2}$; U_A=velocity of ball (m/s); U_B=velocity of disk (m/s); E'=reduced young's modulus (Pa); α=pressure viscosity coefficient (m^2/N), where $\alpha=(0.6+0.965\ log_{10}\eta'_0)\times10^{-8}$; $\eta'_0=\eta_0\times10^3 Pa.s$ [59]; ω=constant load (N); k = ellipticity parameter = 1, for point contact. The film thickness results as a function of temperature are shown in **Figure 7** on the right y-axis.

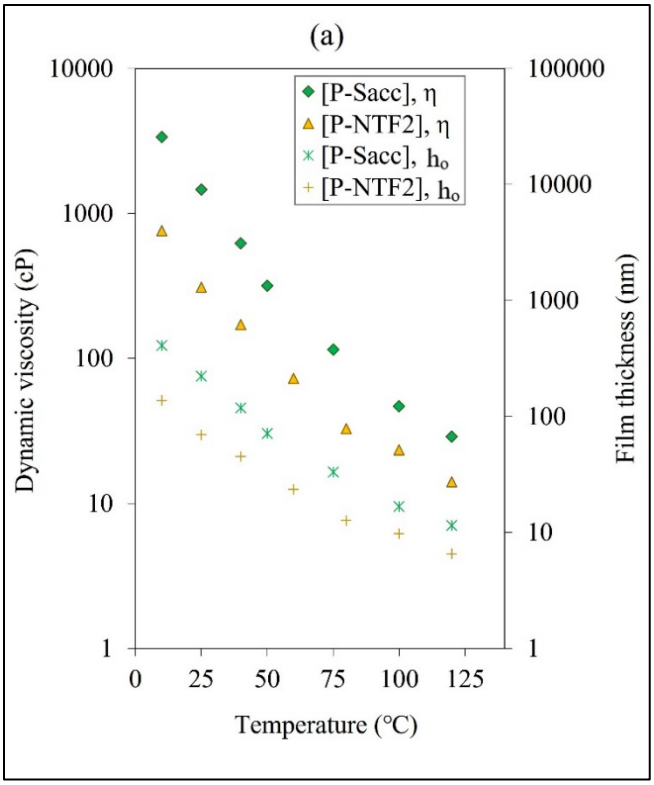

Figure 7. Dynamic viscosity (η) and film thickness (h_o) vs. temperature graph for ILs on a logarithmic scale

In **Figure 7**, it is observed that, as the temperature increased from 10 °C to 120 °C, the viscosity of [P-Sacc] decreased, and the corresponding film thickness decreased from 409 nm to 10.2 nm. For [P-NTF2], the film thickness decreased from 137 nm to 6.5 nm over this temperature range. At all temperatures, the film thickness of [P-Sacc] was significantly larger than that of [P-NTF2], particularly at lower temperatures.

The lambda ratio (λ) between the minimum film thickness (h_0) and the roughness (σ^*) provides information about the lubricating regime [11]. σ^* is the composite Root Mean Square (RMS) roughness of the two surfaces, $\sigma^* = \sqrt{R_{q^1}^2 + R_{q^2}^2}$, where R_{q^1} and R_{q^2} are the RMS roughness values for the ball and the disk, respectively. Generally, boundary lubrication occurs if λ is less than 1. The mixed lubrication regime is expected if $1 \leq \lambda \leq 3$, and, for a value above 3, hydrodynamic lubrication and full separation of the mating surfaces are expected [53].

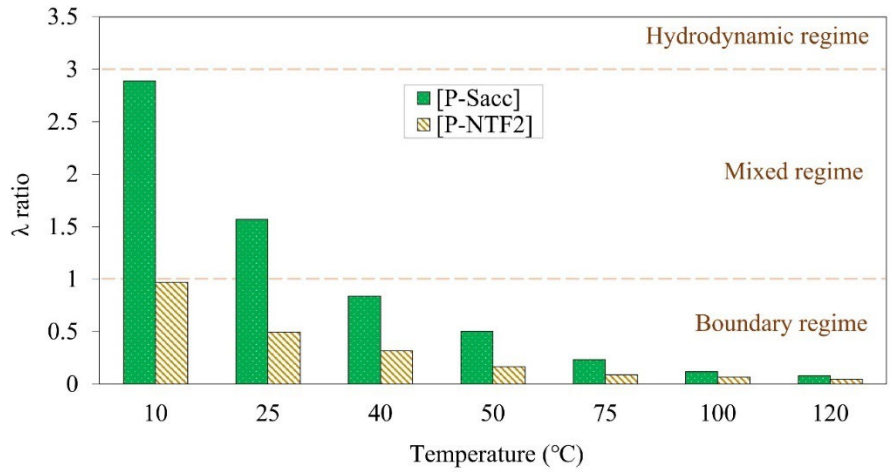

Figure 8. The λ ratio vs. temperature for [P-Sacc] and [P-NTF2]

Figure 8 shows the variation in the lambda (λ) ratio with respect to temperature. The film thickness decreased with increasing temperature and was higher for [P-Sacc] than for [P-NTF2] (**Figure 7**), so the λ ratio exhibited the same trends. The λ ratio for [P-Sacc] at 10 °C and 25 °C indicated the mixed lubrication regime. The physical meaning of $1 \leqslant \lambda \leqslant 3$ is that the film thickness is comparable to the roughness of the surfaces, meaning that some of the load is supported by asperities and some by lubricant. Therefore, in our experimental conditions, [P-Sacc] can provide a film thickness that is able to separate some of the asperities at 10 and 25 °C. Above 25 °C, the λ ratio indicates the test would run in the boundary lubrication regime ($\lambda < 1$) where the load is supported by asperity contacts with adsorbed lubricant molecules. On the other hand, for [P-NTF2], the λ ratio indicated operation in the boundary lubrication regime ($\lambda < 1$) at all temperatures.

3.5 Wettability

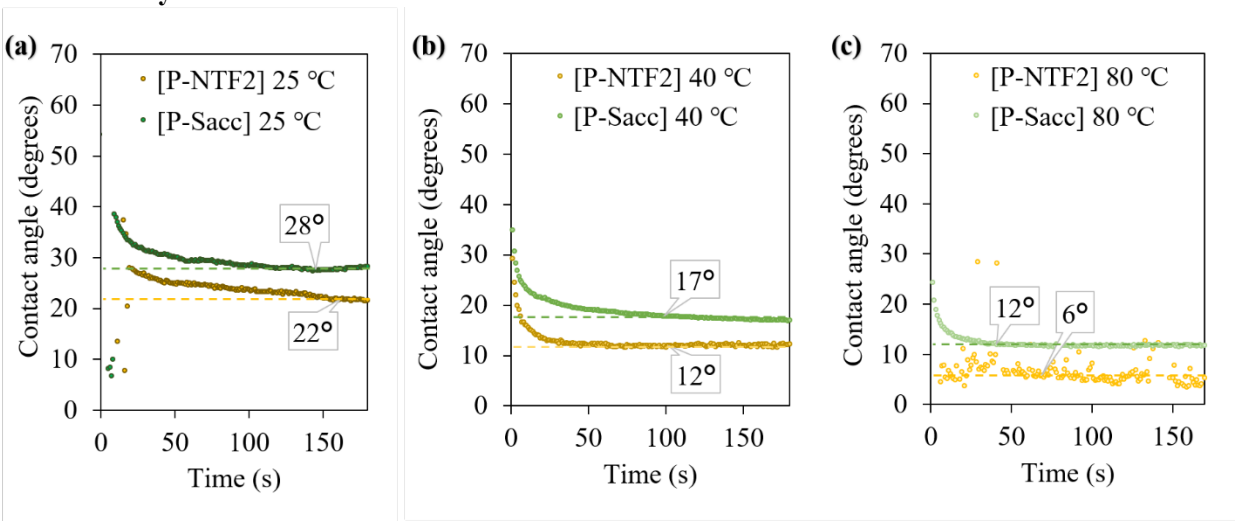

Figure 9. The contact angles of [P-Sacc] and [P-NTF2] at (a) 25 °C, (b) 40 °C, (c) 80 °C. Data call out boxes and the horizontal lines indicate the steady state contact angle (average over the last 20 seconds).

Figure 9 (a-c) shows the contact angle of the ILs at different temperatures. In all the cases, the steady-state contact angles were below 30º, meaning good wettability and strong adhesion to the steel surface. Both ILs

having hydrocarbon cations created an adsorption layer and exhibited low contact angle [33, 61, 62]. However, with an increase in temperature, the physicochemical and surface properties of the IL-steel system changed, which potentially affected their contact angles. In our study, the steady-state contact angles of [P-Sacc] at 25 ℃, 40 ℃, and 80 ℃ were 28, 17, and 12 degrees, respectively. On the other hand, for [P-NTF2], the values were 22, 12, and 6 degrees. The [P-Sacc] contact angle reached steady state within 140, 100, and 40 seconds at 25, 40, and 80 ℃; [P-NTF2] followed a similar trend. Overall, the contact angles were smaller and reached steady state more quickly at higher temperatures. This could be because the lower viscosity of the ILs at higher temperatures facilitated the spreading of liquid molecules [63]. This also explains the higher contact angle of [P-Sacc] than [P-NTF2] since the viscosity of [P-Sacc] was higher than [P-NTF2].

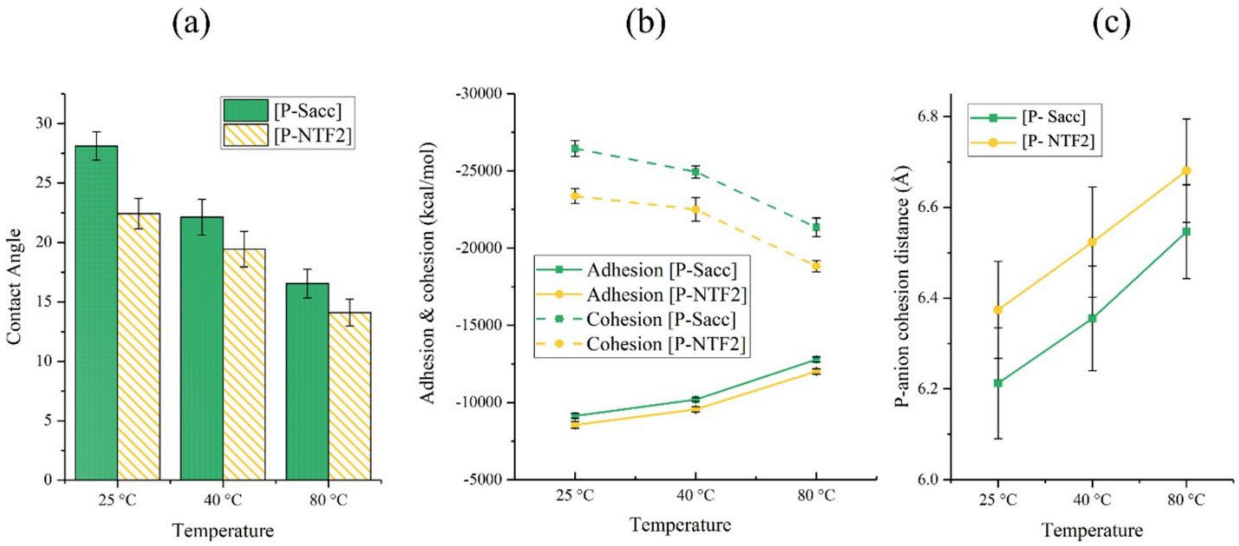

Figure 10. (a) Contact angle, (b) adhesion/cohesion energy, and (c) P-anion cohesion distance for [P-Sacc] and [P-NTF2] on the iron surface calculated from simulations at different temperatures.

MD simulations were carried out for the same two P-RTILs characterized experimentally. As shown in **Figure 10 (a),** the average simulated contact angles for [P-Sacc] at 25 ℃, 40 ℃ and 80 ℃ were 28, 22, and 16 degrees. On the other hand, for [P-NTF2], the contact angles were 22, 19, and 14 degrees. The simulation contact angles were larger than those in experiment due to the limited size and time scales of the simulations. However, despite their differences, in both simulations and experiments, contact angle decreased with temperature and [P-Sacc] had a larger contact angle than [P-NTF2].

Wettability is determined by the relative strengths of adhesion and cohesion energies. These energies were characterized in the simulations. The adhesion energy between P-RTILs and the surface was obtained by calculating the total energy between Fe atoms and all atoms in the P-RTILs. The cohesion energy between cations and anions in P-RTILs was obtained by calculating the total interaction energy between the atoms in cations and the atoms in anions. A negative adhesive or cohesive energy corresponds to net attraction. **Figure 10 (b)** shows the adhesion and cohesion energies for [P-Sacc] and [P-NTF2]. It has been reported that strong adhesion and weak cohesion together will lead to lower contact angle [34]. Since the cohesive energy is much larger than the adhesive energy in all cases, cohesion dominates the contact angle trends for these P-RTILs.

For both ILs, the cohesive energy decreases with temperature, consistent with the contact angle which is smallest at the highest temperature. High temperature results in more thermal vibration and greater distance between the ions. In a previous study, we showed that attractive cohesion interactions are primarily between the P atom in the cation and the atoms in the anion [38]. The average distance between the P atom in the cation and the center-of-mass of the anion, shown in **Figure 10 (c)**, increases with temperature, consistent with the cohesive energy and contact angle trends. Further, the cohesion energy is larger and the cation-anion distance is smaller for [P-Sacc] than for [P-NTF2] at all temperatures. This can be explained by the molecular structure of the anions since the [NTF2] anion is larger with fluorine chains that hinder the approach of the cation. These results are consistent with the larger contact angle of [P-Sacc] in both simulations and experiments.

3.6 Corrosion behavior

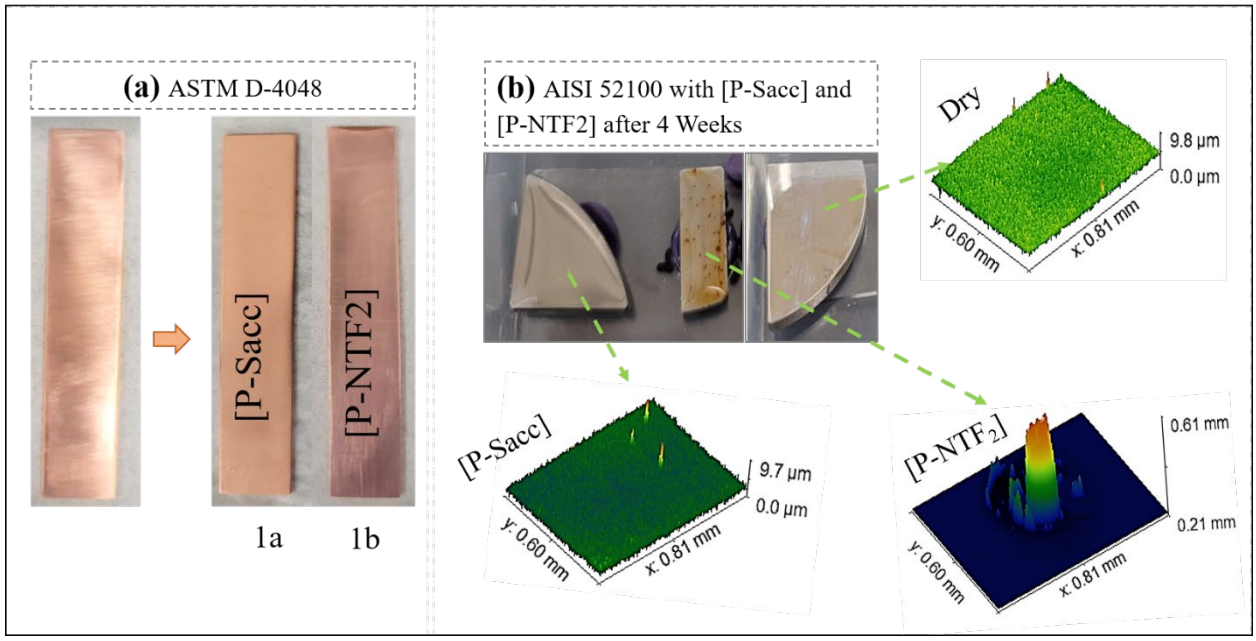

Figure 11. (a) Copper strip test and **(b)** AISI 52100 corrosion inspection result over four weeks (3-D profilometer images are upside-down for better visibility of pitting)

Figure 11 (a) shows the corrosion behavior of the ILs measured by the copper strip test as per the ASTM D-4048 standard. It was observed from inspection that the copper sample with [P-Sacc] exhibited slight discoloration, barely noticeable (1a) whereas the copper sample with the [P-NTF2] was slightly tarnished (1b) after the test. This indicates that [P-Sacc] possibly causes less corrosion than [P-NTF2]. Further measurements were performed on AISI 52100 to characterize the corrosion behavior of both ILs with steel surfaces. **Figure 11 (b)** shows the topography of the AISI 52100 steel after leaving the surfaces in contact with ILs for 4 weeks. It was observed that the steel surface with bio-based [P-Sacc] was unchanged after four weeks. In contrast, significant pitting occurred on the sample with [P-NTF2]. The presence of fluorine in [NTF_2] likely accelerated corrosion [11, 64].

3.7 Tribological performance

Tribological tests with the P-RTILs were performed at 10 °C, 25 °C, 40 °C, 80 °C, and 120 °C. The friction and wear results, and post-test analyses are discussed in the following subsections.

3.7.1 Frictional behavior

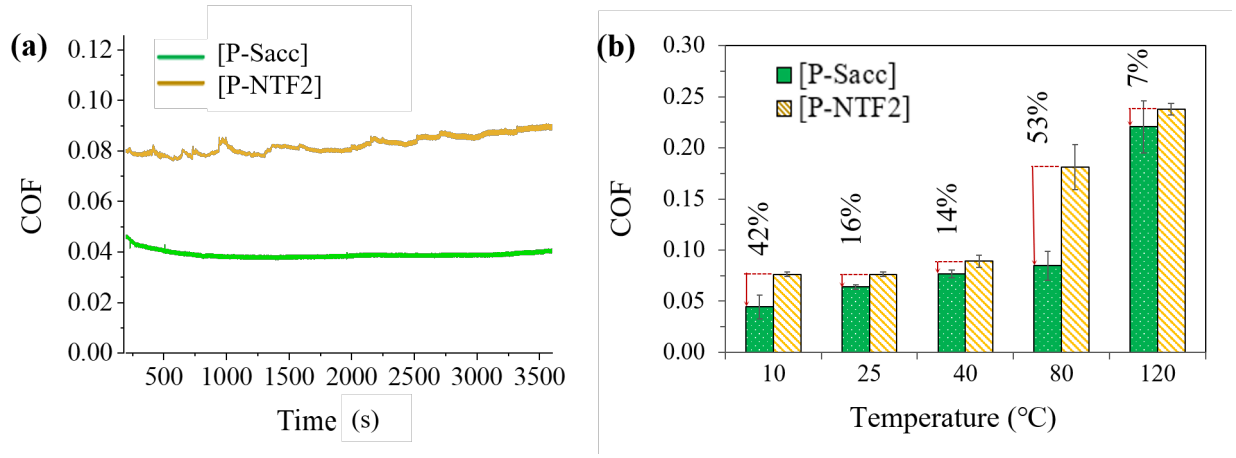

Figure 12. (a) COF of [P-Sacc] and [P-NTF2] over 1 h at 10 °C, and (b) average COF of [P-Sacc] and [P-NTF2] at five different temperatures.

Figure 12 (a) shows the COF values for [P-Sacc] and [P-NTF2] measured over 1 hour at 10 °C. It is observed that the COF was more stable and lower for [P-Sacc] than for [P-NTF2] throughout the test duration. **Figure 12 (b)** shows the average COF at different temperatures. As shown in **Figure 12 (b),** the average COFs for [P-Sacc] were 42, 16, 14, 53, 7% less than for [P-NTF2] at 10, 25, 40, 80, and 120 °C, respectively. The high COF for [P-NTF2] at 80 °C could be attributed to its low viscosity (32.8 mPa·s) and corresponding thin film (12.7 nm) at this temperature. Comparatively, [P-Sacc] exhibited higher viscosity at 80 °C (108 mPa·s), which provided a thicker lubricant film (30.0 nm). At 120 °C, the film thickness for both ILs was small (11.5 nm and 6.5 nm for [P-Sacc] and [P-NTF2], respectively) and therefore the COF for both ILs increased to above 0.2). With an increase in temperature, when the film thickness became 12.7 nm or less, friction increased significantly. Under these conditions, [P-Sacc] was able to provide better protection against friction, possibly because of the double ring aromatic structure of the saccharinate anion [10].

Table 2 gives the friction coefficients for [P-Sacc] and [P-NTF2] ILs at different temperatures and the percent change in COF relative to room temperature value. It is observed that the COF for [P-Sacc] was 31% less at 10 °C than at room temperature, whereas, at 40, 80, and 120 °C, the COF was 18, 32, and 245% higher than at room temperature, respectively. For [P-NTF2] the COFs at 10 and 25 °C were similar, whereas the COF was 17, 138 and 213% higher than at room temperature at 40, 80, and 120 °C respectively. As observed in earlier studies, a high COF for ILs above 100 °C may be due to the loss of lubricant at the interface [65, 66].

Table 2. COF and percent difference in COF with respect to the COF room temperature

[P-Sacc]			[P-NTF2]		
Temperature (°C)	COF	% diff. w.r.t. 25 °C	Temperature (°C)	COF	% diff. w.r.t. 25 °C
10	0.044	-31.20%	10	0.076	0.30%

25	0.064	0.0%	25	0.076	0.0%
40	0.076	18.80%	40	0.089	17.10%
80	0.085	32.80%	80	0.181	138.2%
120	0.221	245.3%	120	0.238	213.2%

3.7.2 Wear results for [P-Sacc] and [P-NTF2]

Figure 13 (a, b) shows 3D topography images of the worn disk and ball surfaces for both ILs after testing at 10°C. The wear track for [P-Sacc] was smoother (Rq=156.2 nm) compared to that for [P-NTF2] (Rq=220.1 nm). **Figure 13 (c)** shows representative 2D wear track profiles for [P-Sacc] and [P-NTF2] after testing at 10 °C. The depth of the wear track for [P-Sacc] was smaller than that for [P-NTF2]. **Figure 13 (d)** depicts the wear volumes of the steel surfaces at different temperatures and shows that wear volume increased with increasing temperature. Up to 80 °C, the volumetric wear was 0.2 mm^3-0.3 mm^3 for [P-Sacc] and 0.25 mm^3-0.35 mm^3 for [P-NTF2]. Then, at 120 °C, the wear volume increased significantly and reached approximately 0.6 mm^3 for both ILs.

Table 3 gives the percent change of wear volume for [P-Sacc] and [P-NTF2] relative to the wear volume at room temperature. Volumetric wear loss for [P-Sacc] was 3% less at 10 °C compared to room temperature, whereas, at 40, 80, and 120 °C, volumetric wear increased by 22, 33, and 146%. Comparatively, [P-NTF2] experienced 10% less wear at 10 °C compared to 25 °C, whereas at 40, 80, and 120 °C, volumetric wear increased by 9, 17, and 95%. The percent change of wear volume for [P-NTF2] was smaller than that for [P-Sacc]. However, the magnitude of the wear volume was higher for [P-NTF2] than [P-Sacc] at all temperatures except 120 °C.

Table 3. Wear volume and percent difference in wear with respect to wear at room temperature

[P-Sacc]			[P-NTF2]		
Temperature (°C)	Wear volume (mm^3)	% diff w.r.t. 25 °C	Temperature (°C)	Wear volume (mm^3)	% diff w.r.t. 25 °C
10	0.225	-3.43%	10	0.262	-9.97%
25	0.233	0.0%	25	0.291	0.0%
40	0.284	21.9%	40	0.318	9.28%
80	0.310	33.0%	80	0.339	16.5%
120	0.573	145.9%	120	0.566	94.5%

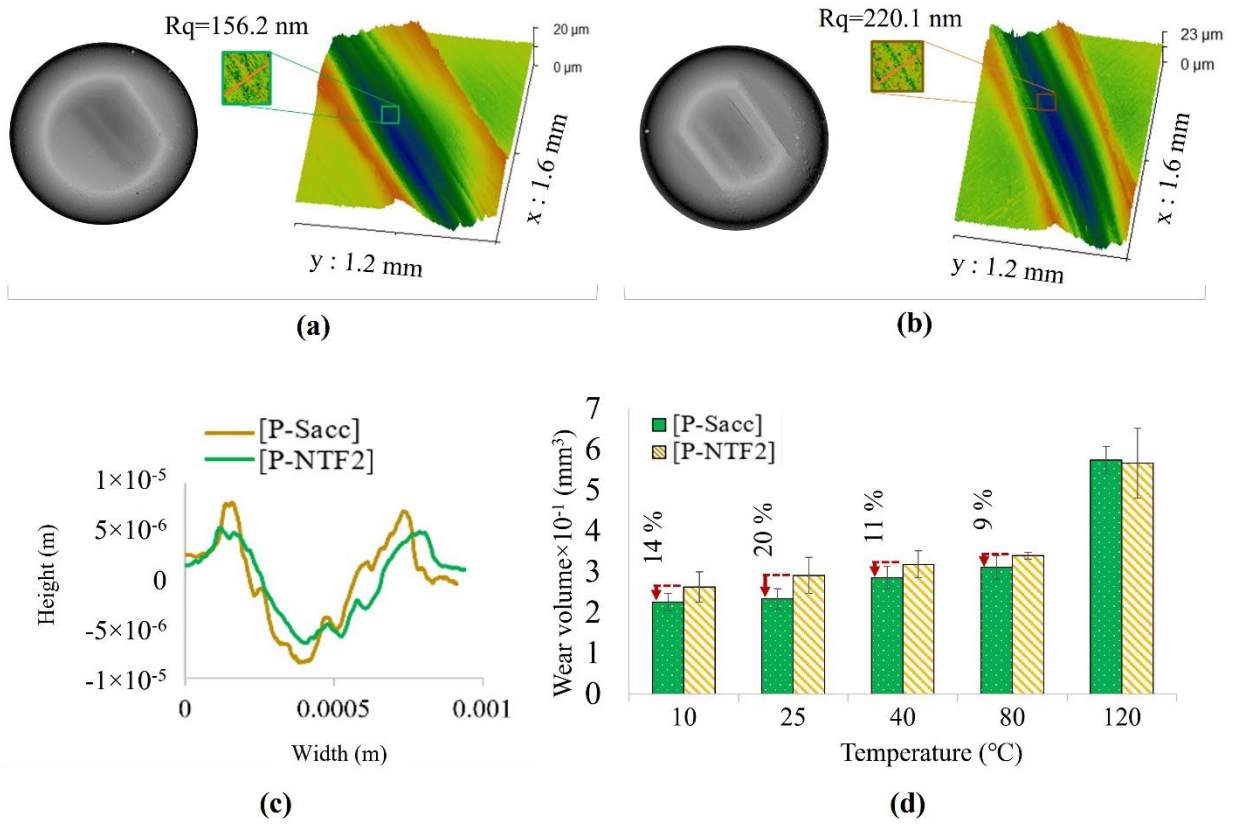

Figure 13. 3D wear tracks from a representative disk and ball from ball-on-disk tests at 10 °C with **(a)** [P-Sacc] and **(b)** [P-NTF2], **(c)** 2D wear profiles from wear tracks at 10 °C, and **(d)** volumetric wear measured on the disk surfaces with [P-Sacc] and [P-NTF2] at five different temperatures.

Figure 14 shows scanning electron micrographs of the wear tracks formed on the AISI 52100 disk surfaces after tribo-tests for both ILs at different temperatures. It is observed from **Figure 14 (a-b)** that there are ridges on the sides of the wear track that indicate the harder ball plowed through the surface of the softer disk during sliding. These patterns are characteristic of abrasive wear. The abrasive marks in **Figure 14 (a)** are less prominent than in **Figure 14 (b),** meaning [P-Sacc] protected the surface better than [P-NTF2]. Also, the root mean square roughness (Rq) of 156.2 nm in the wear track was smaller for [P-Sacc] than the root mean square roughness of 220.1 nm for [P-NTF2]. This might be explained by the presence of more oxygen and fluorine in [P-NTF2], which might have led to corrosion-assisted wear [67, 68]. At 25 °C (**Figure 14 (b1 and b2)**), 40 °C (**Figure 14 (c1 and c2),** and 80 °C (**Figure 14 (d1 and d2)**), the plowing action and ridge formation became more prominent for both ILs. At 120 °C (**Figure 14 (e)**), the wear tracks for both [P-Sacc] and [P-NTF2] were wider, consistent with the smaller film thickness for both P-RTILs at this temperature.

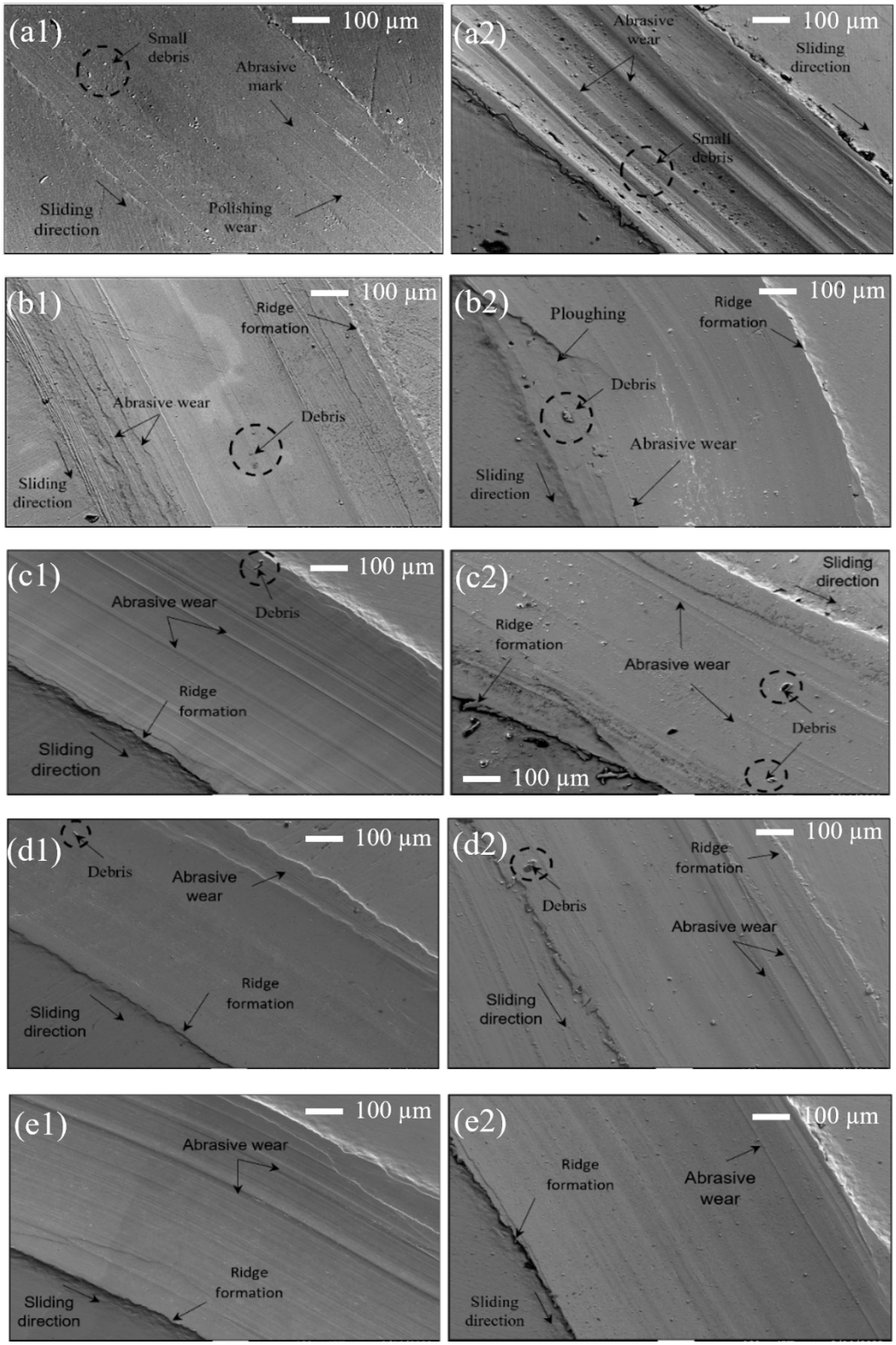

Figure 14. Scanning electron micrographs (x100, 100µm, 15 kV) of the wear tracks of AISI 52100 surfaces from ball-on-disk tests at 10 °C, 25 °C, 40 °C, 80 °C, and 120 °C for (a1-e1) [P-Sacc] and (a2-e2) [P-NTF2].

3.7.3 EDX Analyses on the wear tracks

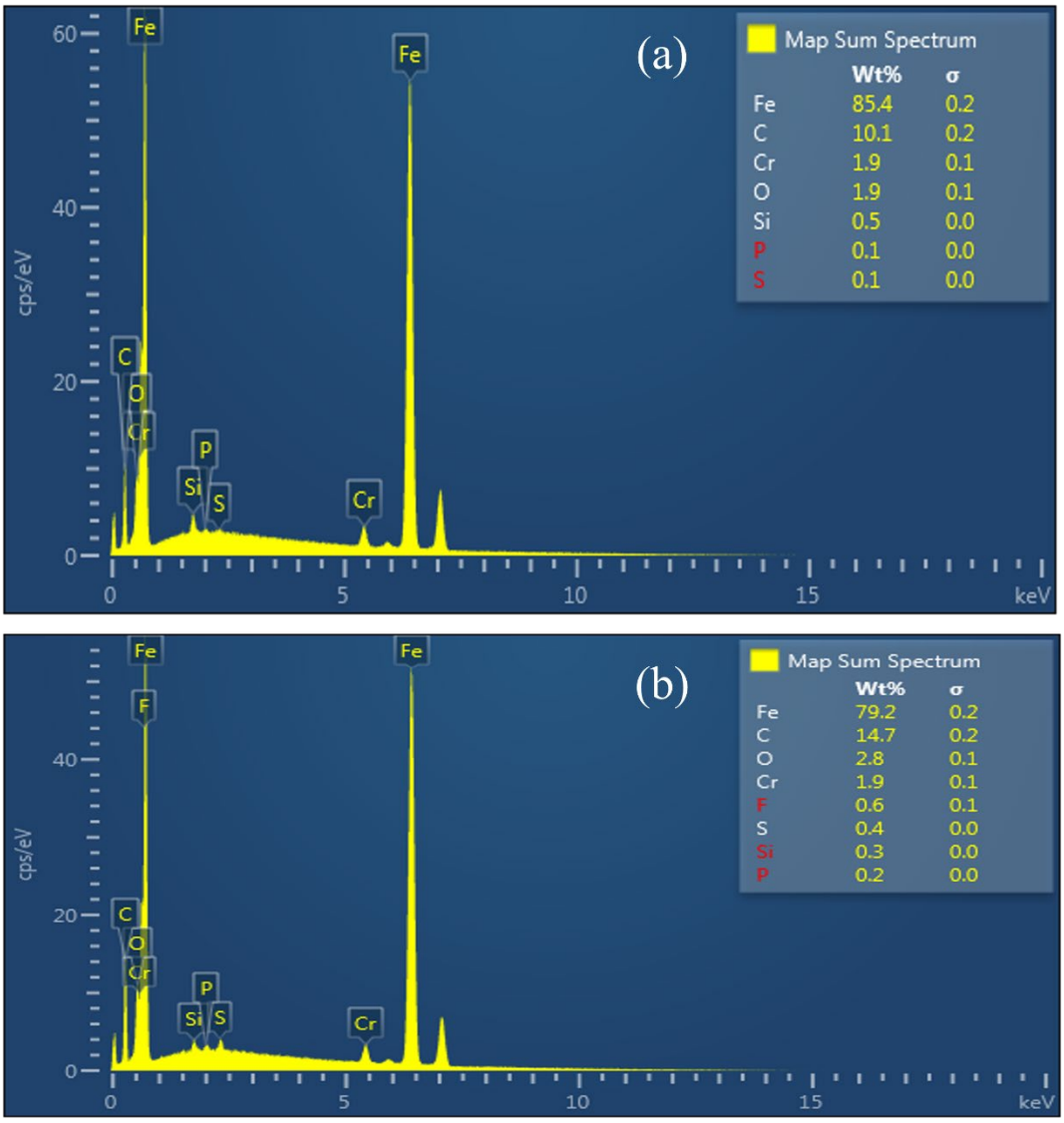

Figure 15. EDX analyses on the wear track of AISI 52100 steel at 10 ℃ with **(a)** [P-Sacc] and **(b)** [P-NTF2] ILs at different temperatures.

EDX analyses were done on the wear tracks as shown in **Figure 15**, and the percentage of different elements is reported in **Table 4**. It is observed that the worn surfaces contain a lower amount of oxygen for [P-Sacc] compared to [P-NTF2] at all temperatures. This is because the [NTF2] anion contains more oxygen atoms than [P-Sacc]. Therefore, when the rubbing action took place, the free electrons emitted from the steel surface made the surface positively charged, which attracted the anions [69]. The [Sacc] anions, having electronegative oxygen and carbon, were able to anchor on the surface and create an adsorption film [70, 71]. Other active elements, such as phosphorus and sulfur, were also present on the surface that could have contributed to adsorption layer formation [21]. In the case of [P-NTF2], the presence of electronegative oxygen and fluorine in the wear track indicates both were able to adsorb to the surface to anchor the [NTF2] anion and create bi-layer structures. Earlier literature on P-RTILs supports this mechanism of bi-layer structure formation [11, 69]. Moreover, oxygen, fluorine, and sulfur are surface-active molecules and could

have chemically reacted with the steel surface [72]. Oxidation of the metallic surface is facilitated by higher temperatures [73]. Therefore, the oxygen content at the surface could have increased with temperature due to oxidation. Further, more sulfur was detected in EDX for the [P-NTF2] than the [P-Sacc], consistent with the greater amount of sulfur in [NTF2] compared to [P-Sacc]. Other surface reactive atoms such as phosphorus was present for both ILs in small percentage (0.1-0.3%). Fluorine was present in the wear track for only [P-NTF2] between (0.6-1.3%).

Table 4. Percentage of elements observed in the worn steel surfaces through EDX analyses.

ILs	Temp (°C)	O (wt.%)	P (wt.%)	S (wt.%)	F (wt.%)	C (wt.%)	Cr (wt.%)	Fe (wt.%)	Others (wt.%)
[P-Sacc]	10	1.9	0.1	0.1	0.0	10.1	1.9	85.4	0.5
[P-Sacc]	25	1.6	0.2	0.1	0.0	12.3	1.8	83.9	0.1
[P-Sacc]	40	1.2	0.2	0.1	0.0	14.9	1.9	81.4	0.3
[P-Sacc]	80	5.1	0.3	0.4	0.0	15.9	2.0	76.1	0.2
[P-Sacc]	120	4.7	0.1	0.2	0.0	5.60	2.2	86.0	1.2
[P-NTF2]	10	2.8	0.2	0.4	0.6	14.7	1.9	79.2	0.2
[P-NTF2]	25	1.9	0.2	0.3	0.9	12.5	2.0	81.9	0.3
[P-NTF2]	40	5.3	0.3	0.6	1.3	16.8	2.0	73.6	0.1
[P-NTF2]	80	6.2	0.3	0.6	1.0	13.3	1.8	76.5	0.3
[P-NTF2]	120	6.9	0.2	0.4	0.9	10.3	1.9	79.3	0.1

4. Lubrication Mechanisms

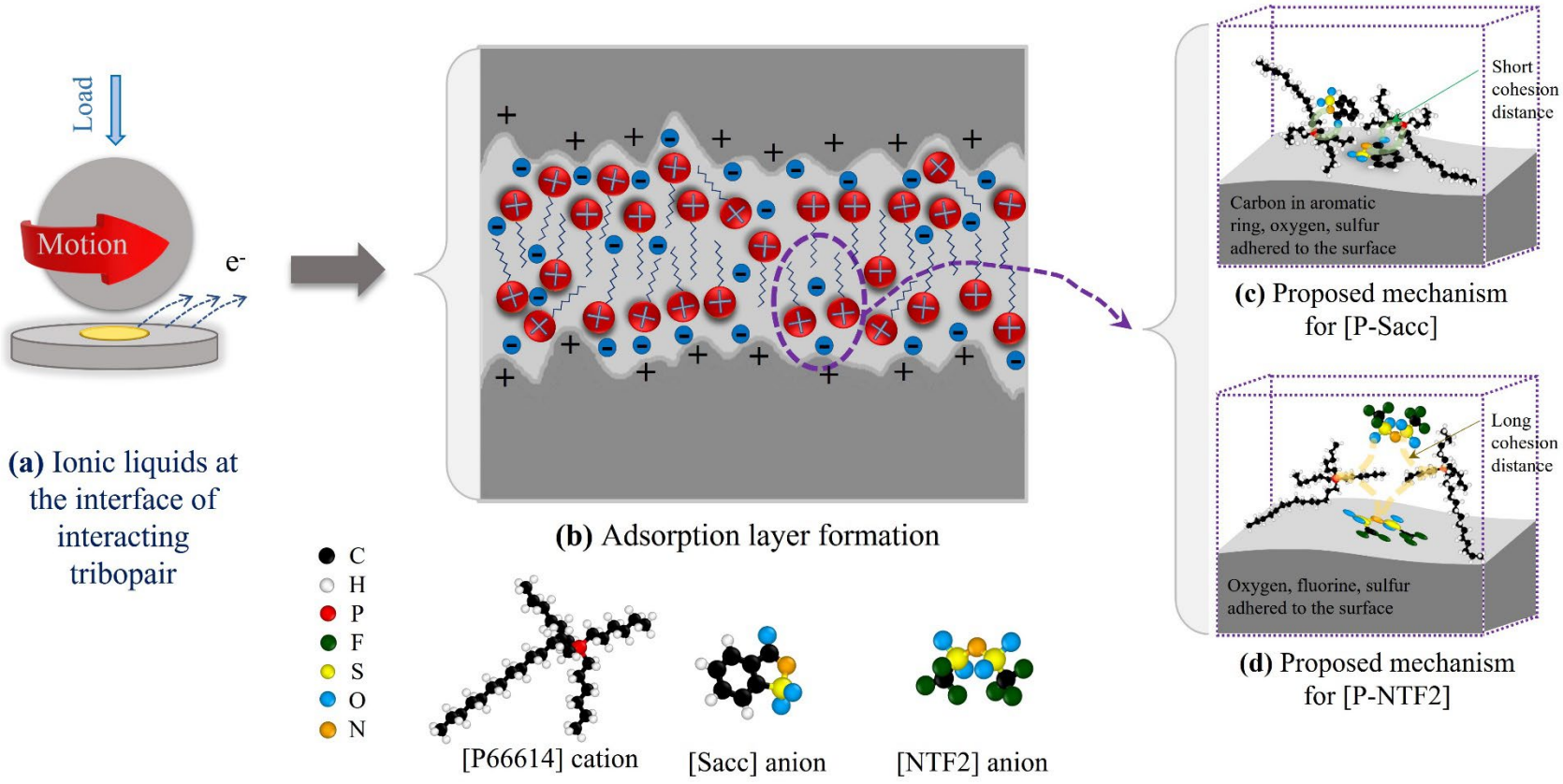

Figure 16. Proposed friction and wear reduction mechanism for [P-Sacc] and [P-NTF2] ILs on steel surfaces

Figure 16 illustrates the lubrication mechanisms of [P-Sacc] and [P-NTF2] based on the analyses so far. First, due to sliding, the metal surface emits free electrons and leaves a positively charged surface that attracts the anion moieties with electrostatic force [74]. Ionic liquids are known to form anion-cation layer-by-layer structures on metal substrates where the anion moiety anchors on the surface [69]. This layered structure protects the surface to reduce friction and wear [11]. The [Sacc] anion, having a cyclic ring-shaped structure with carbon and oxygen, has stronger adhesion to steel than [NTF2] [70]. The simulations confirmed that [P-Sacc] had stronger adhesion to Fe than [P-NTF2]. An atom-by-atom analysis showed that the stronger adhesion of the [Sacc] was due to the interactions between C atoms in the aromatic ring and the Fe atoms in the surface (Figure S2 (b)). As a result, [P-Sacc] having aromatic ring structure has a higher probability to form a thicker tribofilm on metal surfaces, possibly leading to a lower friction and wear rate.

Another possible mechanism could be the formation of reactive tribofilm, which has been discussed in the literature [11, 75]. During tribotesting, some ionic liquid molecules can dissociate and react with Fe in the steel substrate and create a tribochemical film. The presence of P in the EDX measurements of the wear tracks shows that such tribofilm could have been formed and may contribute to minimizing friction [76]. Similarly, the presence of fluorine, oxygen, and sulfur in the wear track could also be partially responsible to tribochemical reaction film formation. Fluorine, oxygen, and sulfur accelerate corrosion and may increase friction and wear [11, 75, 77]. Especially at higher temperatures, the activity of electronegative groups is promoted and could have contributed to poorer tribological performance [73]. Moreover, tribocorrosion could have affected the performance of the ILs at higher temperatures, although this would require further investigation to confirm. [P-Sacc] having less sulfur and no fluorine, experienced less corrosion and, due to the aromatic ring structure of the anion, offered better friction and wear performance overall [77].

5. Conclusions

In this study, [P-Sacc] and [P-NTF2] ILs were used to study their physicochemical and surface wetting properties and their effects on the lubrication mechanism. The main conclusions from this study are the following.

- Based on their long-term thermal stability ($t_{0.99}$) and pour point, it was observed that both ILs were thermally stable and flowable between 10 °C to 120 °C.
- The density of [P-Sacc] (0.93 kg/m^3- 0.97 kg/m^3) was less than that of [P-NTF2] (1.02 kg/m^3- 1.07 kg/m^3) at all temperatures. Therefore, [P-Sacc] would be beneficial for use in aerospace, automobile, or turbine applications in which weight is a concern.
- The thermal expansion coefficient of [P-Sacc] (5.6×10^{-4} °C^{-1}) was less than that of [P-NTF2] (6.80×10^{-4} °C^{-1}), suggesting [P-Sacc] may be better for temperature-sensitive applications.
- The COF of both ILs increased with an increase in temperature. This was attributed to a decrease in viscosity and film thickness, leading to a reduced λ ratio.
- Simulation-based analysis of cohesion and adhesion showed that [P-Sacc] had higher cohesive interaction strength and smaller cation-anion distance than [P-NTF2]. The cohesion interaction energy was smaller at higher temperatures, and the ionic distance increased. This explained the contact angle trends and suggested another factor contributing to friction and wear performance.
- The corrosion behavior of biobased [P-Sacc] was significantly better than [P-NTF2] due to the absence of fluorine. In a 28-day study, pitting marks on the surface with [P-NTF2] were prominent, whereas, for [P-Sacc], no pitting was observed.

- It was observed that, at lower temperatures (10-40 °C), both P-RTILs provided excellent friction and wear protection for steel surfaces. At 80 °C, both P-RTILs offered excellent wear protection, but the COF was lower for [P-Sacc] than for [P-NTF2]. Therefore, [P-Sacc] can be consider as a lubricant for wind turbines applications.
- The higher viscosity and more electronegative carbon and oxygen in [P-Sacc] enabled it to create a protective adsorption film that provided superior lubrication performance than [P-NTF2] overall.

In wind turbine applications, a thermally stable, halogen-free, bio-based IL is of interest. Here we have shown that [P-Sacc], a bio-based IL derived from edible sugar, exhibited superior friction, wear, and corrosion performance over a wide range of temperatures compared to a halogen-based IL. Therefore, bio-based [P-Sacc] could be utilized in lubrication applications due to its corrosion and tribological performance.

Acknowledgments

The authors would like to acknowledge the help from Dr. Joel Desormeau to access the SEM, Mr. Brian Nagy for helping with sample disk preparation, and Soumya Sikdar for assisting with several experiments. Authors also wants to acknowledge the generous help of Mr. Tanzil Mahmud and Dr. Stephen Spain during the ^{1}H and ^{13}C NMR experiments.

Declaration of Interest

There is no conflict of interest to declare

Funding information

The authors appreciate the financial support of the National Science Foundation (Grant No. CMMI-2010205 and 2010584).

References:

[1] A. Haines, K.R. Smith, D. Anderson, P.R. Epstein, A.J. McMichael, I. Roberts, P. Wilkinson, J. Woodcock, J. Woods, Policies for accelerating access to clean energy, improving health, advancing development, and mitigating climate change, The Lancet 370 (2007) 1264, https://doi.org/10.1016/S0140-6736(07)61257-4.

[2] T. Kåberger, Progress of renewable electricity replacing fossil fuels, Global Energy Interconnection 1 (2018) 48, https://doi.org/10.14171/j.2096-5117.gei.2018.01.006.

[3] P. Vennestrøm, C.M. Osmundsen, C. Christensen, E. Taarning, Beyond petrochemicals: the renewable chemicals industry, Angewandte Chemie International Edition 50 (2011) 10502, https://doi.org/10.1002/anie.201102117.

[4] C.M. Fernandes, A.H. Battez, R. González, R. Monge, J. Viesca, A. García, R.C. Martins, J.H. Seabra, Torque loss and wear of FZG gears lubricated with wind turbine gear oils using an ionic liquid as additive, Tribology International 90 (2015) 306, https://doi.org/10.1016/j.triboint.2015.04.037.

[5] U.E. Supply, 20% wind energy by 2030. 2009.

[6] M.A. Gutierrez, M. Haselkorn, P. Iglesias, The lubrication ability of ionic liquids as additives for wind turbine gearboxes oils, Lubricants 4 (2016) 14, www.doi.org/10.3390/lubricants4020014.

[7] S. Lindenberg, 20% Wind Energy By 2030: Increasing Wind Energy¿ Contribution to US Electricity Supply. diane publishing, 2009.

[8] D.K. Singh, J. Kurien, A. Villayamore, Study and analysis of wind turbine gearbox lubrication failure and its mitigation process, Materials Today: Proceedings 44 (2021) 3976, https://doi.org/10.1016/j.matpr.2020.10.047.
[9] A.K. Kasar, C.J. Reeves, P.L. Menezes, The Effect of Particulate Additive Mixtures on the Tribological Performance of Phosphonium-based Ionic Liquid Lubricants, Tribology International (2021) 107300, https://doi.org/10.1016/j.triboint.2021.107300.
[10] C.J. Reeves, A.K. Kasar, P.L. Menezes, Tribological Performance of environmental friendly ionic liquids for High-Temperature Applications, J Clean Prod (2021) 123666, https://doi.org/10.1016/j.jclepro.2020.123666.
[11] M.H. Rahman, A. Khajeh, P. Panwar, M. Patel, A. Martini, P.L. Menezes, Recent progress on phosphonium-based room temperature ionic liquids: Synthesis, properties, tribological performances and applications, Tribology International 167 (2022) 107331, https://doi.org/10.1016/j.triboint.2021.107331.
[12] A. Khajeh, M.H. Rahman, T. Liu, P. Panwar, P.L. Menezes, A. Martini, Thermal decomposition of phosphonium salicylate and phosphonium benzoate ionic liquids, Journal of Molecular Liquids (2022) 118700, https://doi.org/10.1016/j.molliq.2022.118700.
[13] T. Liu, P. Panwar, A. Khajeh, M.H. Rahman, P.L. Menezes, A. Martini, Review of Molecular Dynamics Simulations of Phosphonium Ionic Liquid Lubricants, Tribology Letters Underr revision (2022), www.doi.org/10.1007/s11249-022-01583-6.
[14] C.J. Reeves, A. Siddaiah, P.L. Menezes, Ionic Liquids: A Plausible Future of Bio-Lubricants, Journal of Bio-and Tribo-Corrosion 3 (2017) 18, https://doi.org/10.1007/s40735-017-0076-1.
[15] C.J. Reeves, A. Siddaiah, P.L. Menezes, Tribological study of imidazolium and phosphonium ionic liquid-based lubricants as additives in carboxylic acid-based natural oil: advancements in environmentally friendly lubricants, J Clean Prod 176 (2018) 241, https://doi.org/10.1016/j.jclepro.2017.12.099.
[16] C.J. Reeves, A. Siddaiah, P.L. Menezes, Friction and Wear Behavior of Environmentally Friendly Ionic Liquids for Sustainability of Biolubricants, Journal of Tribology 141 (2019), https://doi.org/10.1115/1.4042872.
[17] R. Monge, R. González, A.H. Battez, A. Fernández-González, J. Viesca, A. García, M. Hadfield, Ionic liquids as an additive in fully formulated wind turbine gearbox oils, Wear 328 (2015) 50, https://doi.org/10.1016/j.wear.2015.01.041.
[18] K.I. Nasser, J.M.L. del Río, E.R. López, J. Fernández, Synergistic effects of hexagonal boron nitride nanoparticles and phosphonium ionic liquids as hybrid lubricant additives, Journal of Molecular Liquids 311 (2020) 113343, https://doi.org/10.1016/j.molliq.2020.113343.
[19] E. Cigno, C. Magagnoli, M.S. Pierce, P. Iglesias, Lubricating ability of two phosphonium-based ionic liquids as additives of a bio-oil for use in wind turbines gearboxes, Wear 376 (2017) 756, https://doi.org/10.1016/j.wear.2017.01.010.
[20] E. Cigno, Tribological Study of High Performance Bio-Lubricants Enhanced with Ionic Liquids for Use in Wind Turbines. Rochester Institute of Technology, 2016.
[21] G. Chen, F. Li, C. Zhang, X. Guo, Z. Yang, Q. Yu, B. Yu, M. Cai, D. Tian, Effect of two halogen-free ionic liquids with different anions on the tribological properties of TC4, Journal of Molecular Liquids 343 (2021) 117627, www.doi.org/10.1016/j.molliq.2021.117627.
[22] M. Stout, Wind Power, Renewable Energy World, 2013, https://www.renewableenergyworld.com/wind-power/protecting-wind-turbines-in-extreme-temperatures/#gref.
[23] R. Errichello, J. Muller, National Renewable Energy Lab., Golden, CO (United States); GEARTECH, Albany, California, 1994, https://www.nrel.gov/docs/legosti/old/7076.pdf.
[24] K. Kaur, S. Srivastava, Artificial sugar saccharin and its derivatives: role as a catalyst, RSC Advances 10 (2020) 36571, https://doi.org/10.1039/D0RA05974A
[25] A. Manoj, A.K. Kasar, P.L. Menezes, Tribocorrosion of porous titanium used in biomedical applications, Journal of Bio-and Tribo-Corrosion 5 (2019) 1, www.doi.org/10.1007/s40735-018-0194-4.

[26] V.M. Egorov, D.I. Djigailo, D.S. Momotenko, D.V. Chernyshov, I.I. Torocheshnikova, S.V. Smirnova, I.V. Pletnev, Task-specific ionic liquid trioctylmethylammonium salicylate as extraction solvent for transition metal ions, Talanta 80 (2010) 1177, www.doi.org/10.1016/j.talanta.2009.09.003.
[27] R. Errichello, S. Sheng, J. Keller, A. Greco, National Renewable Energy Lab.(NREL), Golden, CO (United States), 2012.
[28] T.J. Wooster, K.M. Johanson, K.J. Fraser, D.R. MacFarlane, J.L. Scott, Thermal degradation of cyano containing ionic liquids, Green Chemistry 8 (2006) 691, https://doi.org/10.1039/B606395K.
[29] P.L. Menezes, M. Nosonovsky, S.P. Ingole, S.V. Kailas, M.R. Lovell, Tribology for scientists and engineers. Springer, 2013, 10.1007/978-1-4614-1945-7.
[30] C. Roland, S. Bair, R. Casalini, Thermodynamic scaling of the viscosity of van der Waals, H-bonded, and ionic liquids, Journal of chemical physics 125 (2006) 124508, www.doi.org/10.1063/1.2346679.
[31] A. Pensado, M. Comunas, J. Fernández, The pressure–viscosity coefficient of several ionic liquids, Tribology Letters 31 (2008) 107, www.doi.org/10.1007/s11249-008-9343-0.
[32] A. Marmur, C. Della Volpe, S. Siboni, A. Amirfazli, J.W. Drelich, Contact angles and wettability: towards common and accurate terminology, J Surface Innovations 5 (2017) 3, www.doi.org/10.1680/jsuin.17.00002.
[33] L. Matczak, C. Johanning, E. Gil, H. Guo, T.W. Smith, M. Schertzer, P. Iglesias, Effect of cation nature on the lubricating and physicochemical properties of three ionic liquids, Tribology International 124 (2018) 23, https://doi.org/10.1016/j.triboint.2018.03.024.
[34] T. Liu, M.H. Rahman, P.L. Menezes, A. Martini, Effect of Ion Pair on Contact Angle for Phosphonium Ionic Liquids, J The Journal of Physical Chemistry B (2022), www.doi.org/10.1021/acs.jpcb.2c01989.
[35] L. Martínez, R. Andrade, E.G. Birgin, J.M. Martínez, PACKMOL: a package for building initial configurations for molecular dynamics simulations, Journal of computational chemistry 30 (2009) 2157, https://doi.org/10.1002/jcc.21224.
[36] W.L. Jorgensen, D.S. Maxwell, J. Tirado-Rives, Development and testing of the OPLS all-atom force field on conformational energetics and properties of organic liquids, Journal of the American Chemical Society 118 (1996) 11225, https://doi.org/10.1021/ja9621760.
[37] L.S. Dodda, I. Cabeza de Vaca, J. Tirado-Rives, W.L. Jorgensen, LigParGen web server: an automatic OPLS-AA parameter generator for organic ligands, Nucleic acids research 45 (2017) W331, https://doi.org/10.1093/nar/gkx312.
[38] C.Y. Maghfiroh, M. Misto, W. Maulina, A. Arkundato, Parameters (□,□) of Lennard-Jones for Fe, Ni, Pb for Potential and Cr based on Melting Point Values Using the Molecular Dynamics Method of the Lammps Program, IOP Conf. Series: Journal of Physics: Conf. Series, www.doi.org/10.1088/1742-6596/1491/1/012022.
[39] S. Plimpton, Fast parallel algorithms for short-range molecular dynamics, Journal of computational physics 117 (1995) 1, https://doi.org/10.1006/jcph.1995.1039.
[40] A.K. Kasar, K.P. Watson, B. D'Souza, P.L. Menezes, Role of B2O3 and CaO in Al2O3 matrix composite: In-situ phases, density, hardness and wear resistance, Tribology International 172 (2022) 107588, https://doi.org/10.1016/j.triboint.2022.107588.
[41] A.K. Kasar, B. D'Souza, K.P. Watson, P.L. Menezes, Role of CuO in Al2O3-B2O3 Composites: In Situ Phases, Density, Hardness, and Wear Resistance, Journal of Tribology 144 (2022) 101704, https://doi.org/10.1115/1.4054401.
[42] M.H. Rahman, P.R. Bhoi, A. Saha, V. Patil, S. Adhikari, Thermo-catalytic co-pyrolysis of biomass and high-density polyethylene for improving the yield and quality of pyrolysis liquid, Energy 225 (2021) 120231, https://doi.org/10.1016/j.energy.2021.120231.
[43] P.R. Bhoi, M.H. Rahman, Hydrocarbons recovery through catalytic pyrolysis of compostable and recyclable waste plastics using a novel desk-top staged reactor, Environmental Technology & Innovation 27 (2022) 102453, https://doi.org/10.1016/j.eti.2022.102453.

[44] M.H. Rahman, Catalytic Co-pyrolysis of Pinewood and Waste Plastics for Improving the Selectivity of Hydrocarbons and the Quality of Pyrolysis Oil, MS (2020), https://digitalcommons.georgiasouthern.edu/etd/2108/.
[45] U.o.C.L. Angeles, 2017, http://www.chem.ucla.edu/~harding/IGOC/F/five_zone_analysis.html.
[46] R.M. Silverstein, G.C. Bassler, Spectrometric identification of organic compounds, Journal of Chemical Education 39 (1962) 546, https://doi.org/10.1021/ed039p546.
[47] A. Deyko, S.G. Hessey, P. Licence, E.A. Chernikova, V.G. Krasovskiy, L.M. Kustov, R.G. Jones, The enthalpies of vaporisation of ionic liquids: new measurements and predictions, Physical Chemistry Chemical Physics 14 (2012) 3181, www.doi.org/10.1039/C2CP23705A
[48] T.L. Cottrell, The strengths of chemical bonds. Butterworths Scientific Publications, 1958.
[49] B. deB, National Bureau of Standards: Washington, DC, 1970.
[50] S.W. Benson, III-Bond energies, Journal of Chemical Education 42 (1965) 502, https://pubs.acs.org/doi/pdf/10.1021/ed042p502?casa_token=Nd4cABXhPE0AAAAA:d-yS70Q5ZT8CcpEgn1Nbe0P-KUL2qpR0VJLkMOj782iDbD3wBZ1Jqrg4CfsmljYoRcNdaQROB3Z8EMPc.
[51] J. Kerr, Bond dissociation energies by kinetic methods, Chemical reviews 66 (1966) 465, https://doi.org/10.1021/cr60243a001.
[52] Q.-L. Yan, M. Künzel, S. Zeman, R. Svoboda, M. Bartošková, The effect of molecular structure on thermal stability, decomposition kinetics and reaction models of nitric esters, Thermochimica Acta 566 (2013) 137, www.doi.org/10.1016/j.tca.2013.05.032.
[53] J. Salgado, J.J. Parajó, J. Fernández, M. Villanueva, Long-term thermal stability of some 1-butyl-1-methylpyrrolidinium ionic liquids, The Journal of Chemical Thermodynamics 74 (2014) 51, https://doi.org/10.1016/j.jct.2014.03.030.
[54] J. Salgado, M. Villanueva, J.J. Parajó, J. Fernández, Long-term thermal stability of five imidazolium ionic liquids, The Journal of Chemical Thermodynamics 65 (2013) 184, https://doi.org/10.1016/j.jct.2013.05.049.
[55] D. Santos, M. Santos, E. Franceschi, C.u. Dariva, A. Barison, S. Mattedi, Experimental density of ionic liquids and thermodynamic modeling with group contribution equation of state based on the lattice fluid theory, Journal of Chemical Engineering Data 61 (2016) 348, www.doi.org/10.1021/acs.jced.5b00592.
[56] O.M. Hussian, Thermal Expansion Coefficient of Lubricant Oils, (2006).
[57] V. Zharkov, On the dependence of the coefficient of thermal expansion on density, Physics of the earth planetary interiors 109 (1998) 79, https://doi.org/10.1016/S0031-9201(98)00115-0.
[58] B.J. Hamrock, D. Dowson, Ball bearing lubrication: the elastohydrodynamics of elliptical contacts; ASME: New York, NY, USA. 1981, https://doi.org/10.1115/1.3253193.
[59] G.W. Stachowiak, A.W. Batchelor, Engineering tribology. Butterworth-heinemann, 2000.
[60] P.L. Menezes, S.V. Kailas, Effect of roughness parameter and grinding angle on coefficient of friction when sliding of Al–Mg alloy over EN8 steel, (2006), www.doi.org/10.1115/1.2345401.
[61] Y. Hedberg, M.-E. Karlsson, E. Blomberg, I.O. Wallinder, J. Hedberg, Correlation between surface physicochemical properties and the release of iron from stainless steel AISI 304 in biological media, Colloids Surfaces B: Biointerfaces 122 (2014) 216, www.doi.org/10.1016/j.colsurfb.2014.06.066.
[62] A.L. Allred, E.G. Rochow, A scale of electronegativity based on electrostatic force, Journal of Inorganic Nuclear Chemistry 5 (1958) 264, www.doi.org/10.1016/0022-1902(58)80003-2.
[63] L. Chen, E. Bonaccurso, Effects of surface wettability and liquid viscosity on the dynamic wetting of individual drops, Physical Review E 90 (2014) 022401, https://doi.org/10.1103/PhysRevE.90.022401.
[64] A.E. Somers, S.M. Biddulph, P.C. Howlett, J. Sun, D.R. MacFarlane, M. Forsyth, A comparison of phosphorus and fluorine containing IL lubricants for steel on aluminium, Physical Chemistry Chemical Physics 14 (2012) 8224, https://doi.org/10.1039/C2CP40736A.
[65] M. Kronberger, V. Pejaković, C. Gabler, M. Kalin, How anion and cation species influence the tribology of a green lubricant based on ionic liquids, Proceedings of the Institution of Mechanical

Engineers, Part J: Journal of Engineering Tribology 226 (2012) 933, www.doi.org/10.1177/1350650113476440.
[66] T. Lai, R. Chen, P. Huang, Temperature dependence of microscale adhesion force between solid surfaces using an AFM, Journal of Adhesion Science and Technology 29 (2015) 133, www.doi.org/10.1080/01694243.2014.977698.
[67] A. Toloei, V. Stoilov, D. Northwood, The relationship between surface roughness and corrosion, ASME International mechanical engineering congress and exposition 56192 (2013) V02BT02A054, https://doi.org/10.1115/IMECE2013-65498.
[68] A.H. Battez, M. Bartolomé, D. Blanco, J. Viesca, A. Fernández-González, R. González, Phosphonium cation-based ionic liquids as neat lubricants: Physicochemical and tribological performance, Tribology International 95 (2016) 118, https://doi.org/10.1016/j.triboint.2015.11.015.
[69] X. Liu, F. Zhou, Y. Liang, W. Liu, Tribological performance of phosphonium based ionic liquids for an aluminum-on-steel system and opinions on lubrication mechanism, Wear 261 (2006) 1174, https://doi.org/10.1016/j.wear.2006.03.018.
[70] D. Yang, X. Du, W. Li, Y. Han, L. Ma, M. Fan, F. Zhou, W. Liu, Facile Preparation and Tribological Properties of Water-Based Naphthalene Dicarboxylate Ionic Liquid Lubricating Additives, Tribology Letters 68 (2020) 1, https://doi.org/10.1007/s11249-020-01323-8.
[71] A. Somers, P. Howlett, J. Sun, D. MacFarlane, M. Forsyth, Phosphonium ionic liquids as lubricants for aluminium-steel. 2010, https://doi.org/10.2495/TD100231.
[72] Y. Zhou, D.N. Leonard, W. Guo, J. Qu, Understanding tribofilm formation mechanisms in ionic liquid lubrication, Scientific reports 7 (2017) 1, https://doi.org/10.1038/s41598-017-09029-z.
[73] C.D. Taylor, B.M. Tossey, High temperature oxidation of corrosion resistant alloys from machine learning, npj Materials Degradation 5 (2021) 1, https://doi.org/10.1038/s41529-021-00184-3.
[74] S. Hu, Y. Zhang, T. Shao, Study of electrostatic potential induced by friction, Proc. ESA Annual Meeting on Electrostatics (2014) 1.
[75] V. Sharma, C. Gabler, N. Doerr, P.B. Aswath, Mechanism of tribofilm formation with P and S containing ionic liquids, Tribology international 92 (2015) 353, https://doi.org/10.1016/j.triboint.2015.07.009.
[76] I. Minami, T. Inada, R. Sasaki, H. Nanao, Tribo-chemistry of phosphonium-derived ionic liquids, Tribology letters 40 (2010) 225, https://doi.org/10.1007/s11249-010-9626-0.
[77] Y. Zhou, J. Weber, M.B. Viola, J. Qu, Is more always better? Tribofilm evolution and tribological behavior impacted by the concentration of ZDDP, ionic liquid, and ZDDP-Ionic liquid combination, Wear 432 (2019) 202951, https://doi.org/10.1016/j.wear.2019.202951.

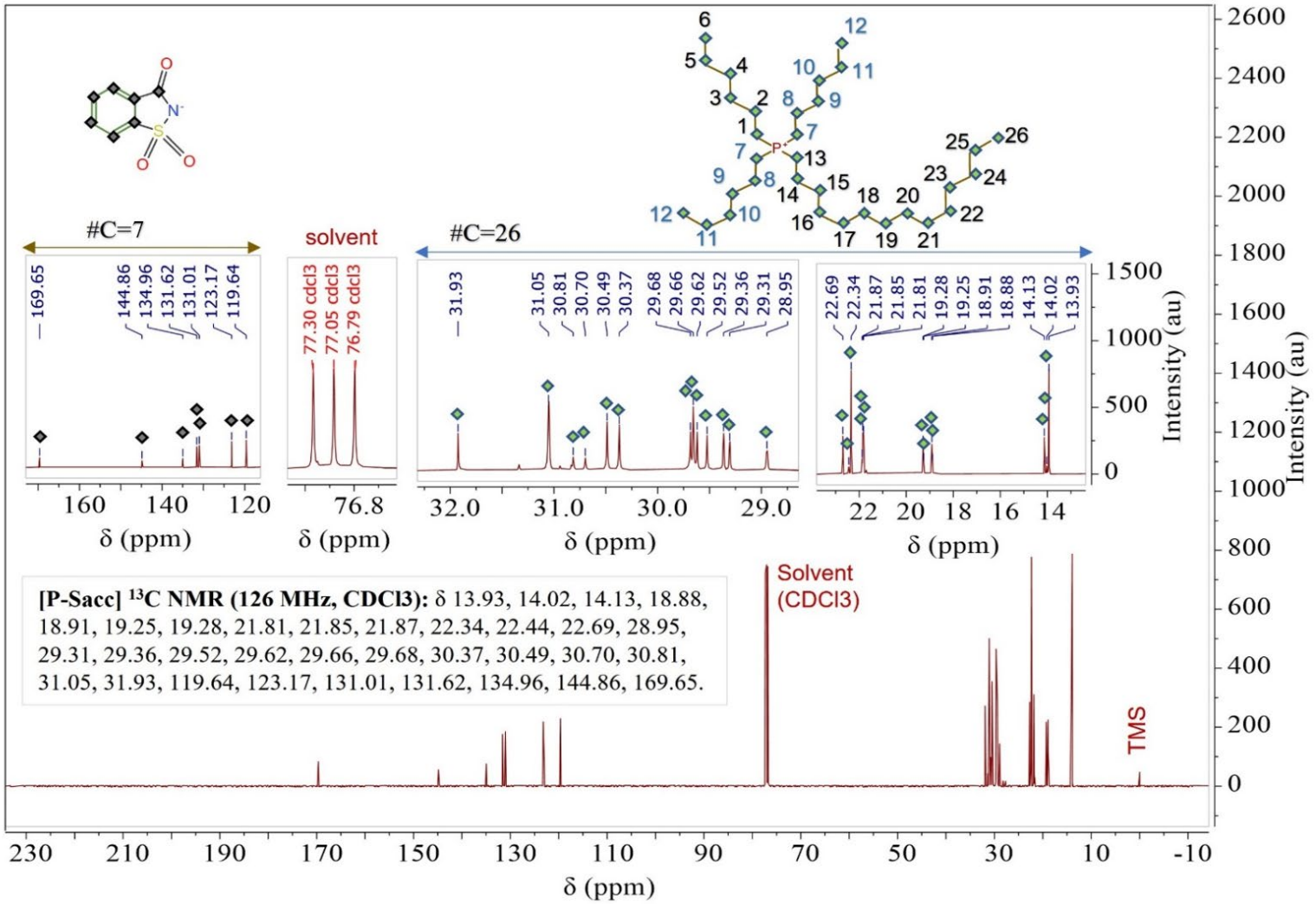

Figure S1: ^{13}C NMR for [P-Sacc]

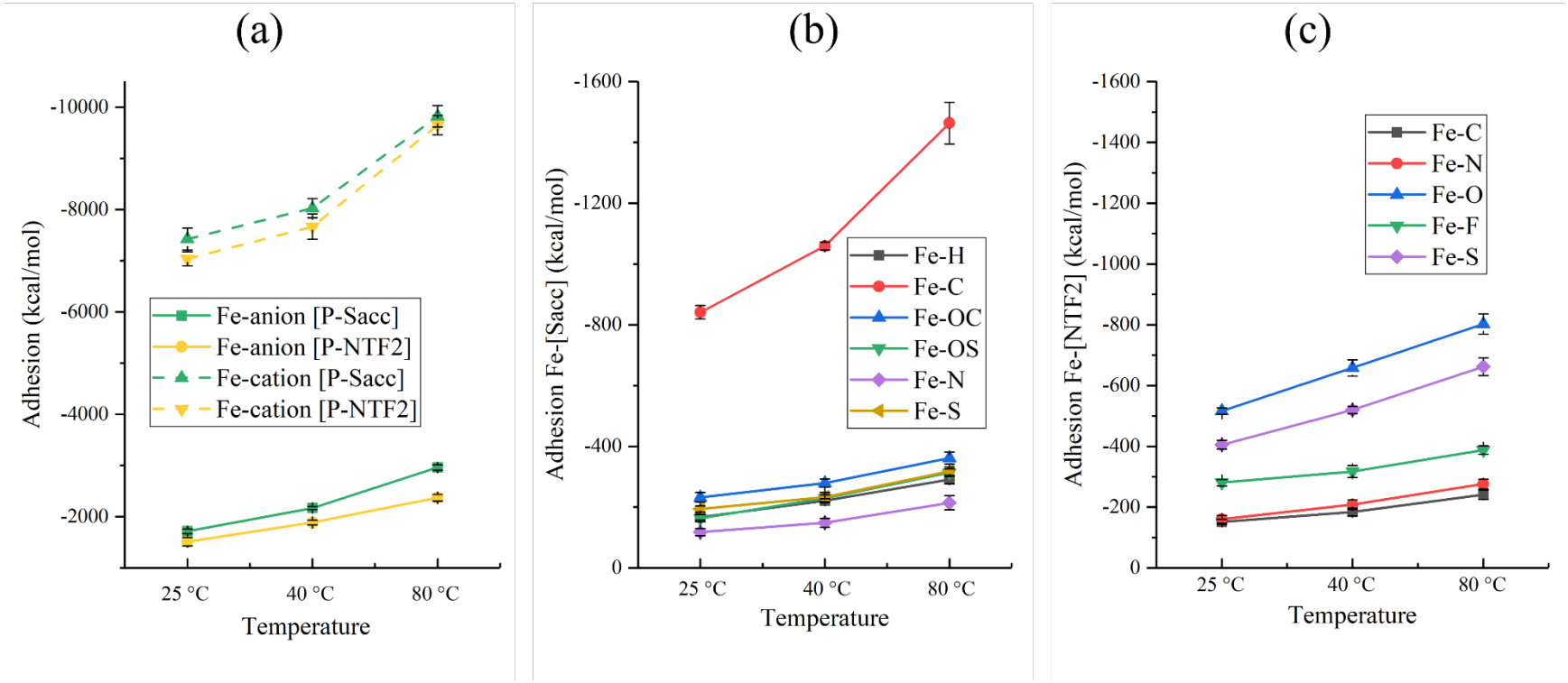

Figure S2: (a) Fe-anion and Fe-cation adhesion energy, (b) Fe-anion adhesion atom-by-atom analysis for [P-Sacc], and (c) Fe-anion adhesion atom-by-atom analysis for [P-NTF2] on the iron surface calculated from simulations at different temperatures.

1